Phase I Final Report for award number **NNX17AJ75G**
R&A Program Name: NASA Innovative Advanced Concepts (NIAC) Phase I
Dates covered by this report: May 9, 2017 to Februrary 8, 2018

Proposal Title: **Dismantling Rubble Pile Asteroids with AoES (Area-of-Effect Soft-bots)**

PI Name: **Jay McMahon**
Institution/address: 431 UCB, University of Colorado, Boulder, CO 80309-0429
Email: jay.mcmahon@colorado.edu
Phone: 303-492-3944

1 Overview of the AoES Project

1.1 The AoES Concept

Area-of-Effect Softbots (AoES) are soft-robotic spacecraft that are designed with a large, flexible surface area to leverage the dynamical environment at rubble pile asteroids. In particular, this surface area allows AoES to use adhesive forces, both naturally arising from van der Waals forces between the AoES and the asteroid regolith, and by using active electroadhesion[33], as well as using SRP forces to provide fuel free orbit and hopping trajectory control. The main purpose of the bus structure is to house a digging and launching mechanism that can liberate and launch asteroid regolith off the surface of the asteroid to be collected in orbit.

It has been well established at this point that van der Waals cohesion plays a major role in holding rubble pile asteroids together[38], becoming a dominant force in microgravity environments[34]. AoES are designed

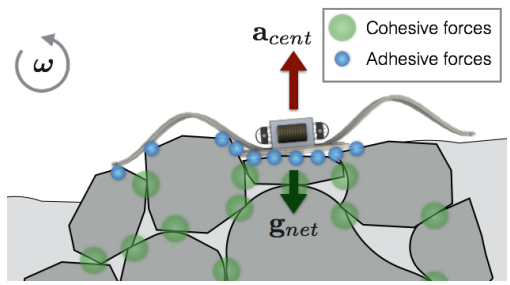

Figure 1: Illustration of the forces on a rubble-pile asteroid.

to take advantage of this force as a controllable means of adhering to the asteroid surface, similar to how geckos [3] walk up walls. This situation is depicted in Fig. 38. In this environment, centripetal accelerations on the surface, caused by the spin of the asteroid, $\boldsymbol{\omega}$, can equal or overcome the net gravitational force at the surface. The cohesive forces between the components of the rubble pile asteroid help to hold it together. AoES will take advantage of similar physics to keep from being launched off the surface by centripetal or reactionary forces.

The initial design for AoES are pictured in Fig. 3. The soft-robotic legs are made of a flexible silicone elastomer, which allows for accommodation of rough asteroid surfaces [1, 7, 36] to keep significant surface area in contact. Furthermore, the legs are actuated using HASEL actuators [**?**] - a necessary component for enabling surface mobility. This is inspired by existing soft robots developed and demonstrated in terrestrial environment [22, 21, 35], e.g. Fig. 39.

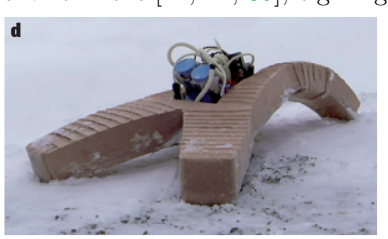

Figure 2: An existing soft robot showing crawling similar to what is proposed [35].

Recent literature has found that rubble pile asteroids should have cohesion on the order of magnitude of 1-10^2 Pa [34, 38]. If spread over a square meter surface area, an adhesive force roughly four orders of magnitude lower between the AoES and the regolith would suffice to keep the AoES design anchored to the surface. AoES will also incorporate electroadhesion [33] to supplement the van der Waals anchoring and mobility.

AoES are designed to support four main modes of operation, as pictured in Fig. 3. The crawling concept is inspired by nature in how animals which rely on adhesion or large surface areas for locomotion (such as slugs or caterpillars) move, as the design in Fig. 39 and others [48, 21] have previously. The high area-to-mass ratio of the AoES design (currently designed to ∼0.1 - 0.5 m^2/kg) also provides another important capability - orbit and hopping trajectory control using SRP forces. This method requires no fuel, and is effectively solar sailing[26]. The AoES can also use the legs to absorb landing energy to preclude Philae-like uncontrolled bounces across the asteroid surface. An internal impulse from the material launching system or by quickly slapping all four soft-robotic legs can be used to start the hop, as

is picture in Fig. 3c. Then, the hop trajectory can be controlled through similar methods as with the orbit control.

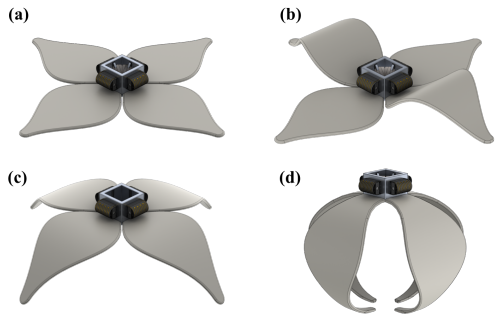

Figure 3: Images of AoES concept in four modes for a) anchoring or solar sailing, b) crawling, c) hopping, d) landing.

The final major component of the AoES design is the capability for AoES to liberate and loft asteroid material. The initial design of the digging/launching mechanism can be seen in Fig. **??**. When the four regolith spades are placed together, they create a bucket that can be accelerated on a track linearly up through the centerline of the bus. When the bucket reaches the end of the track, it will come to a halt but the material inside will escape the open top of the bucket to be lofted from the surface. Note that escape speeds on NEAs of Bennu's size[9] are on the order of 10 cm/s, which can easily be achieved by such a mechanism.

In total, this concept elegantly overcomes many of the difficulties typically encountered when trying to design an ISRU mission which necessitates operating on, and interacting with, the surface of a rubble pile asteroid - in many cases using these perceived difficulties to the advantage of the architecture. This is outlined in Table 1.

Table 1: Challenges of operating at a rubble pile asteroid and unique solutions provided by AoES.

Challenges	**AoES Solutions**
Uncertain sub-surface structure	Adhesive anchoring on surface
Microgravity mobility	Hopping using SRP
Mobility on fast spinners	Crawling with adhesion to prevent being thrown off
Resist reaction forces for digging	Adhesive anchoring over large area
Landing without bouncing	Soft material for energy absorption
Prevent sinking into regolith	Large surface area provides floatation
Precision landing	Orbit control with SRP; subsequent surface mobility
Dusty environment	RTG powered/no solar cells; possibly can shake off dust
Risk of losing spacecraft	Distributed architecture - expensive portion stays in orbit
Initial hop off surface	Impulse from fast actuation or from launching mechanism
Energy for launching regolith	Electrical from RTG - no need for less efficient rocket fuel

1.2 The AoES Mission Context

The mission context for this proposal is to a volatile rich NEA in order to extract water for ISRU, as pictured in Fig. 4. The concept uses a distributed architecture where a processing spacecraft will remain in orbit about the asteroid while one or more AoES will descend to the surface to liberate material from the asteroid and launch it from the surface. The material is then retrieved in orbit by the processing spacecraft, which extracts the water without ever dealing with the dangers of surface operations. Such a mission would

demonstrate that enough water can indeed be harvested from an NEA to make water-based ISRU concepts a reality.

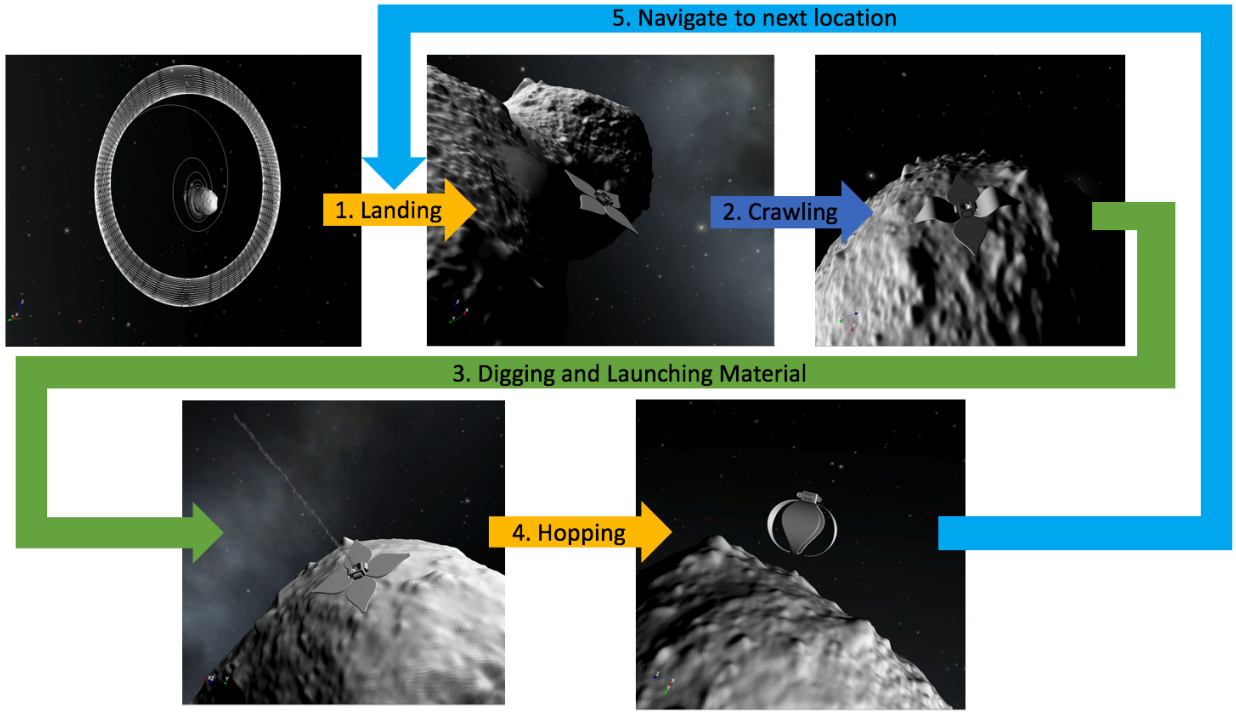

Figure 4: Notional depiction of the AoES concept of operations. This begins with the AoES descending from orbit onto the asteroid using SRP forces (1). Once the AoES has landed in the vicinity of a location of interest, crawling motion enables the AoES to effectively reach the target (2). Surface material can then be dug out and launched away from the surface (3). Once another location of interest has been identified, the AoES hop away from the surface (4) and navigates to the next location of interest (5).

Significant previous work has been carried out on methods for extracting water from asteroid material once the material is acquired.[42, 43] However, the problem of safely gathering material from the surface to process is unsolved at this point. This is the job that AoES are designed to accomplish while being extremely robust to uncertainties about the asteroid environment that can prevent status quo concepts from working.

Many of the fundamental components of the proposed concept and mission architecture already exist or are being developed independently. For example, there are a number of processing ship type concepts such as APIS[42, 43], RAP[52, 17], or ARRM[23]. Soft robotics have been demonstrated, and are an active research area for terrestrial and space[16] applications. Many concepts for mechanically retrieving material from an asteroid have been developed[53]. Retrieving free floating material by an orbiting spacecraft has been previously studied[27]. Thus, if the AoES can be developed, the door to a real ISRU demonstration mission will be opened!

2 The Potential Impact of AoES for NASA and Beyond

The potential impacts of extracting large quantities of water from asteroids throughout the inner solar system are well known and hugely influential to humanity's future exploration and economic existence in space[28]. Ultimately, if this concept is successful at enabling ISRU, the retrieval of water allows for the production of rocket fuel and oxygen for human exploration - launching not only a new commercial opportunity, but a whole new economy.

The unsolved component of the proposed mission architecture is how to get the material from the surface to the processing spacecraft. The beauty of the AoES concept is that it is robust to the many environmental

difficulties and uncertainties we are faced with when attempting to interact with rubble pile surfaces, as discussed in Table 1.

Other status quo concepts may work in certain scenarios, but are not nearly as robust as the AoES solution to these difficulties. ARRM[23] would retrieve a large boulder from the surface of an NEA, but it assumes that the boulder has enough internal strength to avoid being crushed, that the asteroid structure will support the spacecraft during boulder retrieval, and endangers the mission by landing the entire system. Hedgehogs[29] have excellent mobility on the surface, but are not able to operate on fast spinning objects with microgravity, can't control their trajectory once they've hopped, nor do they provide significant anchoring for interaction with or liberation of surface material. Many anchoring concepts[53, 52, 17] make some assumptions on the sub-surface structure of the asteroid to operate or require extremely large structures. Most concepts to date will be subject to bouncing upon landing, like Philae, unless they use thrust all the way to the surface and allow for plume impingement - the exceptions may be OSIRIS-REx and ARRM which both incorporate some shock absorption.

In short, no status quo concept provides the breadth of robustness that AoES can deliver. Given the need for robust surface interaction to make ISRU mission widely successful at many different asteroids, AoES can provide the missing link to a more sustainable future in terms of efficiency, safety, and profitability, for space exploration.

While not the focused concept of this study, AoES would also make a great platform for scientific exploration and planetary defense. Instead of lofting material, AoES could have instruments to analyze the regolith in situ, similar to the Mars rovers. Planetary defense could be achieved by landscaping the orbit to modify the spin, trajectory (through modification of the Yarkovsky effect[5, 8]) and by applying many small impulses from lofting mass (similar to gravity tractor, ion beam, or laser ablation deflection methods), and simply by reducing the mass to reduce the energy of an impact.

In addition to the current aims, AoES are a unique platform for exploring the utility of soft robotics in space: they offer new methods of locomotion, can selectively adhere to a wide range of surfaces through electroadhesion, can modify their orbit using SRP (or drag - for comets or near planets), and offer inherent shock absorption for critical tasks such as landing. After development, when this breadth of capabilities is laid out to a room of engineers and scientists, a remarkable number of applications will certainly be brainstormed in short order!

Finally, the work done in this project can provide a wide array of benefits here on Earth. This research

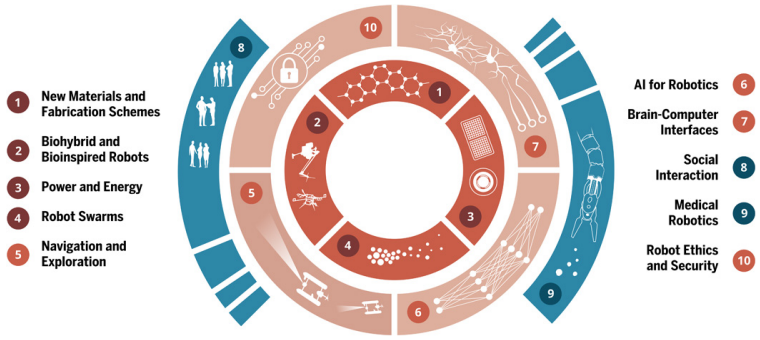

Figure 5: Ten grand challenges of Science Robotics [51].

will continue to build on the body of work [22, 11, 24, 10, 25, 44, 35, 16, 48, 21], concerned with biologically inspired robotics and mobility and soft robotics. The inherent developments resulting from this research will enable robots that can safely maneuver in dynamic and unstructured environments for wide-ranging applications such as search-and-rescue in disaster sites. These efforts will also make progress towards five of the recent grand challenges in robotics [51]: new materials and fabrication schemes; biohybrid and bioinspired robots; power and energy; robot swarms; navigation and exploration; and possibly AI for robotics. This certainly implies there is an upside to this project even if AoES end up being infeasible for their current

mission context.

The combination of these benefits in space and on Earth should provide significant opportunities for public engagement and excitement, especially given the current environment in the space industry in support of commercial development of space. We will use our platform at the University of Colorado to publicize this work as widely as possible.

3 System & Mission Design

3.1 Spacecraft design

The AoES spacecraft is designed as a simple drone that will work in a fleet to mine a small body while being controlled by an orbiting mothership. There are two overarching operational goals that drive this design: 1) to have the ability to control the AoES orbit using solar radiation pressure (SRP), and 2) to be able to safely land on, maneuver about, and manipulate the surface of a small body. These goals are achieved by designing an AoES spacecraft that has a controllable high area-to-mass ratio. Figure 6 shows the preliminary design of the AoES spacecraft.

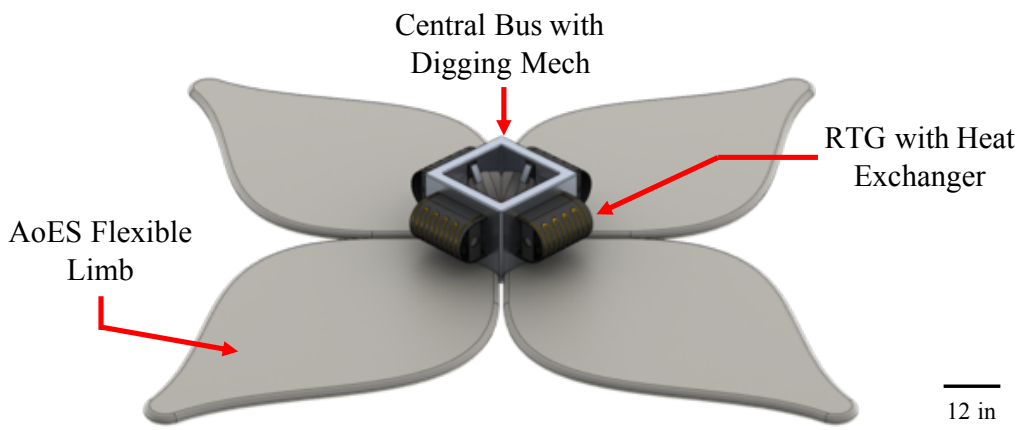

Figure 6: This figure shows the preliminary design of the AoES spacecraft.

3.1.1 Subsystems

As Figure 6 shows, the AoES spacecraft structure is comprised of a central bus and large, petal-shaped limbs. The AoES limbs are a multi-layer composition consisting of a top thermal insulating layer, such as MLI, an internal electronic and actuation layer, and a flexible, durable silicone elastomer (Section 4.1) bottom layer. These limbs are used for directing SRP while in orbit and for maneuvering once on the surface of the small body. The limbs are controlled by bi-directional HASEL (hydraulically amplified self-healing electrostatic) actuators and use a combination of van der Waals adhesion and electroadhesion (Section 4.2, 4.3) to stay anchored to the small body during operations. Figure 7a shows the layout of these components within each limb. The central bus, shown in Figure 7b, is comprised of 1/8 inch thick 6060-T6 Al and is designed around a digging mechanism used to manipulate the surface of the small body. The digging mechanism, shown in Figure 8, is comprised of a titanium (Ti-6Al-4V) regolith spade powered by a drive screw for vertical motion and an electric actuator for digging. Each inner wall of the central bus is equipped with these components to make a fully functional digging subsystem. During excavation of the small body, the AoES lander will first maneuver over the desired location, then simultaneously extend all four spades into the asteroid to secure a sample of regolith, and finally, rapidly drive the four spades to the top of the drive screws effectively

launching the regolith into orbit for collection. With a 20-inch central bus, the AoES spacecraft is capable of excavating up to 15-inch diameter boulders.

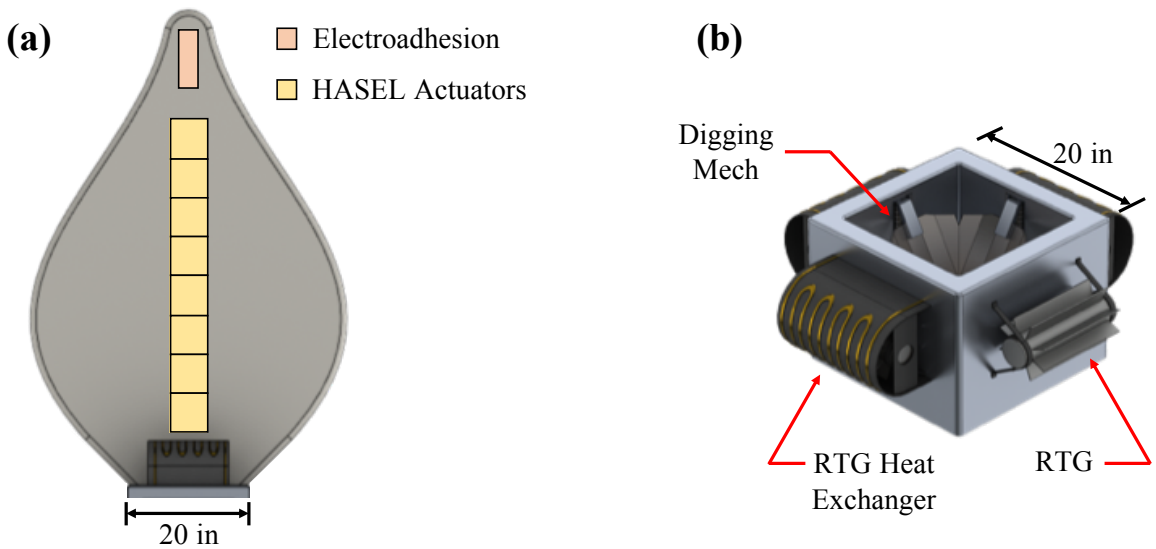

Figure 7: Figure 7a shows the HASEL actuator and electroadhesion layout in the AoES limbs, and Figure 7b shows the central bus of the AoES spacecraft.

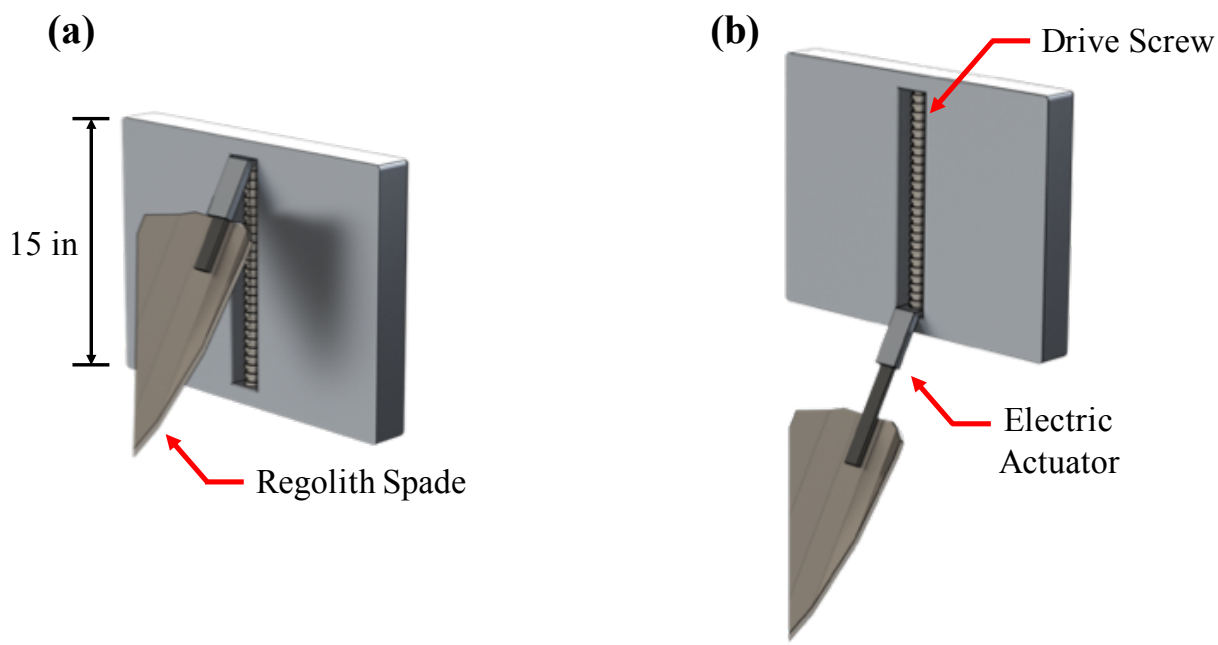

Figure 8: This figure shows one side of the four sided AoES digging mechanism.

From orbit, the AoES spacecraft will use SRP in place of a conventional propulsion system to land on the asteroid. Attitude control and determination (ADC) is provided by a combination of SRP control and

a 3-axis reaction wheel control system based off the Blue Canyon XACT system. This integrated system contains the attitude control laws, orbit propagator, sun sensor, star tracker, and the ability to command and power the reaction wheels and torque rods all in one compact system. Once on the surface of the asteroid, the AoES drone only needs to communicate with the mothership, so a simple ultrahigh frequency (UHF) telecommunication system consisting of the NanoCom 430ANT antenna and NanoCom AX100 transceiver was selected. This system consists of a turnstile antenna consisting of four quarterwave monopole antennae combined in a phasing network forming a single circular polarized antenna. This results in an antenna pattern that is almost omnidirectional with no blind spots which can cause fading during operations. The ISIS Onboard Computer (OBC) supplied by Innovative Solutions in Space was chosen for the command and data handling (CDH) system used to choreograph all of the AoES operations. This system utilizes a 400 MHz ARM9 processor with 64 MB of SDRAM, redundant SD cards for storage, radiation hardened components, and has several years of flight heritage. While strict subsystem requirements are not yet specified, these harware choices yeild realistic mass and power values for system design calcuations.

Due to the dusty and sunlight inhibiting nature of excavating an asteroid, four radioisotope thermoelectric generators (RTGs) are used in place of solar panels as a power source. Each RTG is covered by a heat exchanging shield, shown in Figure 7b, used to both protect the RTGs from debris and leverage the heat output of the RTGs to maintain the necessary temperature within the central bus and limbs. These subsystems result in a practical and reliable preliminary spacecraft design that will be able to efficiently operate in the small body environment.

3.1.2 HASEL Actuators

Movement in the AoES spacecraft will be provided by HASEL actuators - a robust new platform [2, 19] for soft actuator technology that merges two predominant existing technologies - electrically-powered dielectric elastomer actuators (DEAs) and fluidically-powered actuators (e.g. McKibben actuators) - to synergize their strengths while solving many of their issues. While current fluidic actuators are incredibly versatile and capable of numerous modes of actuation [32], they require a supply of pressurized gas or liquid (from a compressor or external reservoir) which must be transported through systems of tubes and control valves. This limits their speed and efficiency, and increases system weight and complexity. Electrically-powered actuators, such as DEAs, are energy efficient, offer high actuation speed, high strain ($\geq 100\%$) [30], and can self-sense their position [20], but they have limited modes of actuation and generally require actuators to be stretched over a frame for effective operation. Furthermore, they are subject to catastrophic failure from dielectric breakdown due to the high electric fields used during operation [13].

HASEL actuators harness an electrohydraulic mechanism to drive shape change of soft active structures, as shown in Figure 9. The basic structure consists of a flexible or stretchable polymer shell filled with a liquid dielectric. Electrodes are placed on the shell on opposing sides of the pouch. By directly applying electrostatic forces to an insulating hydraulic fluid, HASEL actuators combine the versatility of soft fluidic actuators with the fast, efficient, and self-sensing performance of dielectric elastomer actuators. In contrast to soft fluidic actuators, where inefficiencies and losses arise from fluid transport through systems of long tubes and channels, HASEL actuators generate hydraulic pressure locally via electrostatic forces acting on liquid dielectrics, eliminating the need for external reservoirs, pumps, or compressors. In contrast to DEAs, where dielectric breakdown through actuator membranes limits lifetime and reliability, the use of liquid dielectrics in HASEL actuators gives them the ability to self-heal from dielectric failure, as shown in Fig. 1B. Figure 9.C-E highlight previously demonstrated geometries and functionality for these actuators which can be constructed from elastic or inelastic materials to achieve different modes of actuation, self-sense their position, precisely position large or small loads, and be scaled up for increased force production.

3.1.3 Mass and Power

The maximum power draw for each spacecraft subsystem is indicated in Table 2. These numbers represent the worst-case power draw that each subsystem may need, and on average, these requirements will be lower throughout AoES operations (e.g., at steady state the XACT ADC system requires <3 W). As Table 2

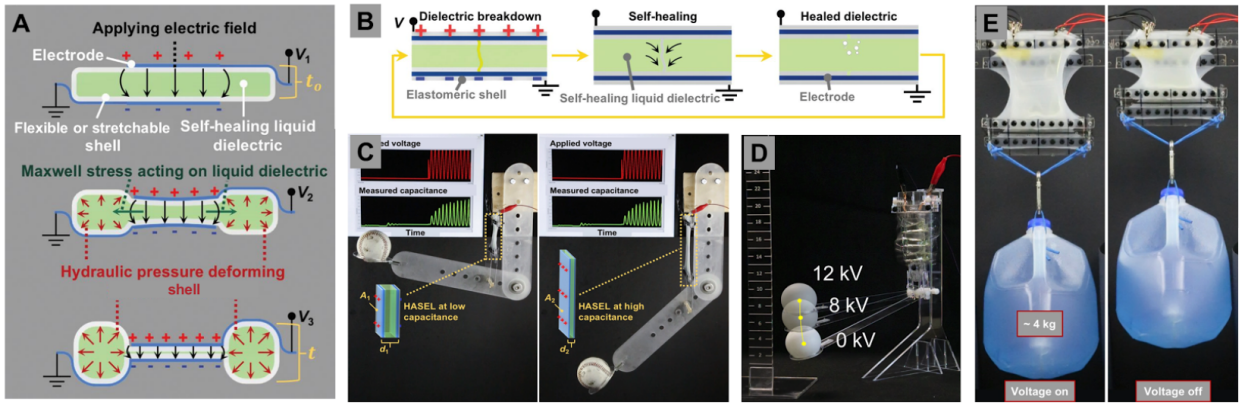

Figure 9: Highlights for HASEL actuators. (A) Principles of operation for HASEL actuators. (B) Mechanism for self-healing in HASEL actuators - after dielectric breakdown, the liquid dielectric reflows into the damaged site and returns to an insulating state. (C) HASEL actuators demonstrate the ability to self-sense their position via capacitance measurements while lifting useful loads. (D) Linearly-contracting flexible Peano-HASEL geometry, which is capable of precisely manipulating a mechanical arm to control position of a table tennis ball. (E) A stack of elastic HASEL actuators in parallel demonstrating increased force production by lifting a gallon of water.

shows, the maximum power required for the AoES to operate, with a 25% margin, is 75.2 W. As previously mentioned, four small RTGs will be used to provide this power requirement. The AoES RTGs, which are currently based on 1:4 scale SNAP-27 RTGs, provide a total power output of 75 W, 1500 W of heat, weigh 20 kg, and use 238-Pu as a fuel source.

It is important to keep in mind that this is a preliminary assessment of the AoES power needs and spacecraft design in general. Further analysis and optimization is needed to fully understand the AoES spacecraft power requirements. For example, the structure subsection power requirement of 40 W, which includes the digging mechanism (20 W, 5 W per spade) and the limb actuators (20 W, 5 W per limb), is based on simple HASEL and electric actuator models. By optimizing the AoES power profile, the total power needs of the AoES spacecraft can be reduced, which in turn will reduce the overall mass of the spacecraft resulting in an increased area-to-mass ratio.

Table 2: AoES Power Chart

Subsystem	Max Power [W]
Structure	40
ADC	16
Telecomm	3.6
CDH	0.55
Propulsion	-
Thermal	-
25% Margin	15.04
TOTAL	75.2

The total mass of the AoES spacecraft as designed is 73.5 kg. This value assumes a limb length of 110 inches and an arbitrary limb thickness of 0.1 inches. Table 3 shows the total mass broken down by each subsystem. The heaviest subsystem by far is the AoES structure, which includes the central bus frame (12.39 kg, assumed to be hollow with 1/8 inch walls), the digging mechanism (8.29 kg), and the limbs (28.44 kg,

assumed to be comprised of only a silicone elastomer). The miscellaneous entry in Table 3 includes extra mass (7% the structure subsystem, based on discussion in Browns *Elements of Spacecraft Design*) to account for cabling and radiation shielding used to connect and protect the various subsystems within the AoES spacecraft. Similar to the AoES power requirements, further analysis and optimization is necessary for a complete understanding of the AoES mass profile. This includes creating a more detailed design of all the AoES subsystems.

Table 3: AoES Mass Chart

Subsystem	Mass [kg]
Structure	49.13
ADC	1.3
Telecomm	0.055
CDH	0.0094
Power	20
Propulsion	-
Thermal	-
Misc	3
TOTAL	73.5

3.1.4 Mission Operations

Throughout its mission, the AoES spacecraft will have to perform a variety of different tasks in many different situations. Figure 10 shows several different operation modes that the AoES spacecraft must be able to execute using the bi-directional HASEL actuators. For example, to maneuver around the surface of the small body (i.e. the crawling mode shown in Figure 10b), the AoES spacecraft will anchor the tip of the limb in the direction of travel using electroadhesion, and then pull itself forward similar to a caterpillar. Alternatively, during decent form orbit (i.e., the landing mode shown in Figure 10d), the AoES spacecraft will fold its limbs under itself to help absorb the impact from landing. The feasibility of these operational modes must be further studied to ensure the AoES spacecraft can successfully complete its mission.

An important aspects of the AoES mission's success is the spacecraft's maneuverability both in orbit and on the surface of the asteroid. The spacecraft's maneuverability in both cases is determined by its area-to-mass ratio, which is in turn determined by the design of the spacecraft's limbs. Different limb designs will favor either orbit control or ground maneuverability. Figure 11 shows a comparison between two contrasting AoES limb shapes. Circular limbs, such as the ones in Figure 11b, result in a higher area-to-mass ratio, which in turn results in better orbit control and higher van der Waals adhesion once on the surface of the small body, and on the contrary, petal limbs, such as the ones in Figure 11a, result in better landing protection and maneuverability on the surface of the small body. Further analysis on the AoES limb shape is necessary to find the optimal solution that satisfies both the orbit and ground maneuverability constraints during the AoES mission.

Regardless of the limb shape, it is advantageous for the AoES spacecraft to have a high area-to-mass ratio. Table 4 and Table 5 show the area-to-mass ratio for a variety of limb lengths, using the mass of the other subsystems shown in Table 3, for both the petal-shaped limbs and the circular-shaped limbs, respectively. As expected, the two tables show that the circular limbs achieve a higher area-to-mass ratio than the petal limbs for the same limb length. Furthermore, the two tables show area-to-mass ratios ranging from approximately 0.1 to 0.2 and the associated limb lengths necessary to achieve these values assuming an arbitrary 0.1 inch limb thickness. An important factor affecting the area-to-mass ratio of the AoES spacecraft is the thickness of its limbs. Further analysis is necessary to determine what the minimum limb thickness can be. In order to maximize the area-to-mass ratio of the AoES spacecraft, the thickness of the limbs needs to be minimized.

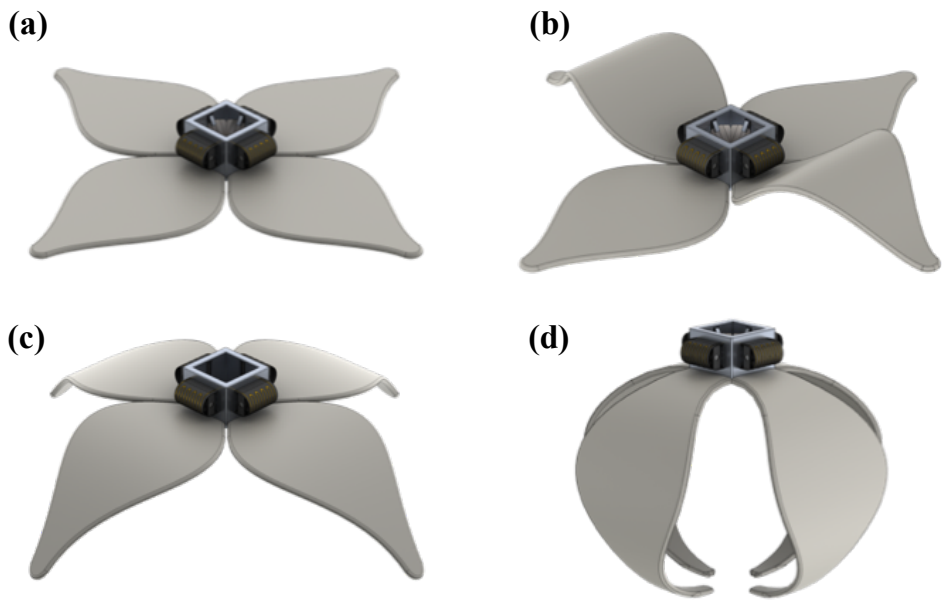

Figure 10: This images shows four of AoES' operational modes: (a) anchoring or solar sailing, (b) crawling, (c) digging, and (d) landing.

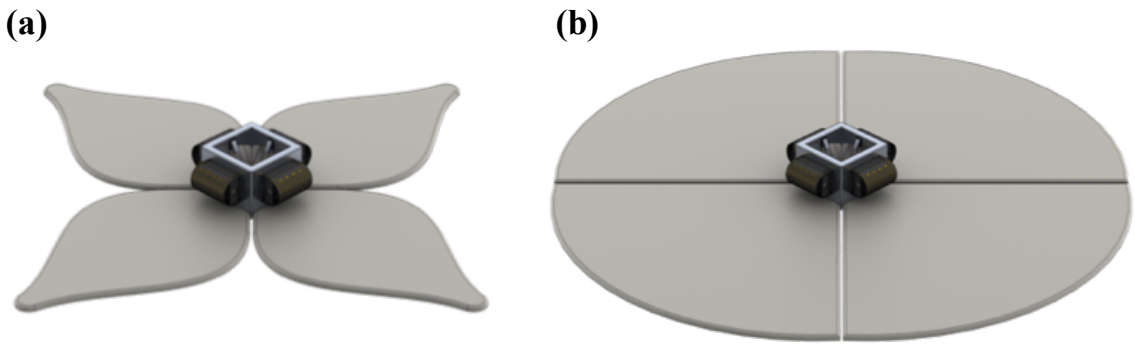

Figure 11: This figure shows different limb configurations for the AoES spacecraft. Figure 11a shows a petal-limb shape that would be better for crawling, and Figure 11b shows a circle-limb shape that provides a better area-to-mass ratio.

Table 4: AoES Petal-Limb Chart

Limb Length [in]	Limb Mass [kg]	AoES Length [ft]	Total Area [m^2]	Total Mass [kg]	A2M
72	4.655	13.67	6.366	63.666	0.1000
80	5.172	15	7.045	65.734	0.1072
110	7.111	20	9.590	73.492	0.1305
265	17.131	45.83	22.740	113.573	0.2002

As this section shows, while a promising preliminary design for the AoES spacecraft has been developed, a much more detailed study of the AoES ADCS and power requirements, mass profile, and limb design,

Table 5: AoES Circle-Limb Chart

Limb Length [in]	Limb Mass [kg]	AoES Length [ft]	Total Area [m^2]	Total Mass [kg]	A2M
32	4.763	7	6.508	64.098	0.1015
80	11.907	15	15.884	92.675	0.1714
110	16.372	20	21.743	110.535	0.1967
115	17.116	20.83	22.720	113.512	0.2002

which are all coupled, is necessary to achieve an optimal design for the AoES spacecraft.

3.2 Dynamics of asteroid mass removal

This section describes the dynamical process an asteroid undergoes as material is removed from its surface [6]. In the long run, the removal of the surface material would cause the spin state of the asteroid to change. The angular velocity dynamics about the center of mass of any rigid body are described by Euler's equation

$$[I]\dot{\boldsymbol{\omega}} = -[\tilde{\boldsymbol{\omega}}][I]\boldsymbol{\omega} + \boldsymbol{L} \tag{1}$$

where $[I]$ is the body's inertia tensor about the its center of mass, $\boldsymbol{\omega}$ is the angular velocity vector, $\boldsymbol{L}$ is the total external torque vector and $[\tilde{(\cdot)}]$ is the tilde operator. The work presented in this section assumes no external torques are applied on the system (i.e., $\boldsymbol{L} = \boldsymbol{0}$). These dynamics describe the rotational motion between an inertial frame $\mathcal{N}$ and the asteroid's body fixed frame $\mathcal{B}$ whose origin is set at the asteroid's center of mass. These frames, and the position vector between their two origins, $\boldsymbol{R}_{CM}$, are presented in Figure 12. The asteroid properties before and after separation are denoted as $(\cdot)^-$ and $(\cdot)^+$, respectively. And the

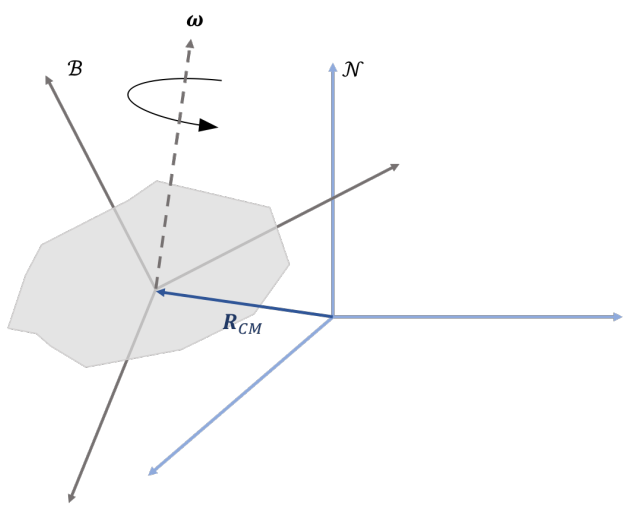

Figure 12: Reference frames in the system

removed mass is denoted as $(\cdot)_\Delta$. The mass and inertia tensor at the moment of separation are (for a frame at the original asteroid center of mass)

$$M^- = M^+ + M_\Delta \tag{2}$$

$$[I^-] = [I^+] + M^+[\tilde{\boldsymbol{r}}^+_{CM}][\tilde{\boldsymbol{r}}^+_{CM}]^T + [I_\Delta] + M_\Delta[\tilde{\boldsymbol{r}}_{CM,\Delta}][\tilde{\boldsymbol{r}}_{CM,\Delta}]^T \tag{3}$$

where the $\boldsymbol{r}_{CM}$ vectors are the position of each new body's center of mass.
The system's total angular momentum prior to separation (in the center of mass frame) is

$$\boldsymbol{H}^- = [I^-]\boldsymbol{\omega}^-. \tag{4}$$

Immediately after separation the total angular momentum includes both rotational and translational elements in it. And, at the moment of separation the new angular velocity is identical for both bodies ($\boldsymbol{\omega}^+ = \boldsymbol{\omega}_\Delta$). Thus

$$\boldsymbol{H}^+ + \boldsymbol{H}_\Delta = \Big([I^+] + [I_\Delta]\Big)\boldsymbol{\omega}^+ + M^+(\boldsymbol{r}^+_{CM} \times \dot{\boldsymbol{r}}^+_{CM}) + M_\Delta(\boldsymbol{r}_{CM,\Delta} \times \dot{\boldsymbol{r}}_{CM,\Delta}). \tag{5}$$

where the $\dot{\boldsymbol{r}}_{CM} = \omega^- \times \boldsymbol{r}_{CM}$ expressions are the linear velocities of the center of mass of each of the objects.
The system's total angular momentum prior to separation (in the center of mass frame) is

$$\boldsymbol{H}^- = [I^-]\boldsymbol{\omega}^-. \tag{6}$$

The following figures present the result of removing 15 boulders from a site on the asteroid Itokawa. Prior to removal the asteroid is a principal axis rotator, aligning its maximum moment of inertia axis with its angular velocity. On the left of Figure 13, the development of the angular velocity is shown and compared to nominal case where Itokawa is locked on a principal axis rotation regime. The right side of this figure shows the motion of the angular velocity projection on the equatorial plane of the asteroid. We note that the principal axis rotation property is lost due to the mass removal. Figure 14 tracks the position of the center of mass of the asteroid as mass is removed from it. The position of the center of mass is compared to the nominal case. We note that the center of mass shifts in position as the mass is removed and that translational velocity is added to the asteroid.

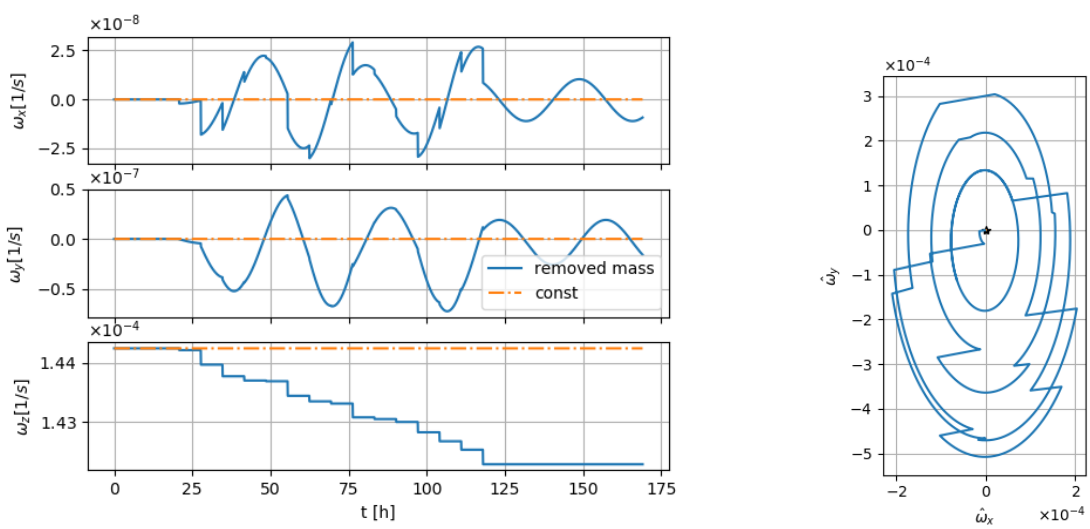

Figure 13: Angular velocity components (left) and projection of the angular velocity on the equatorial plane (right) for asteroid Itokawa undergoing material removal

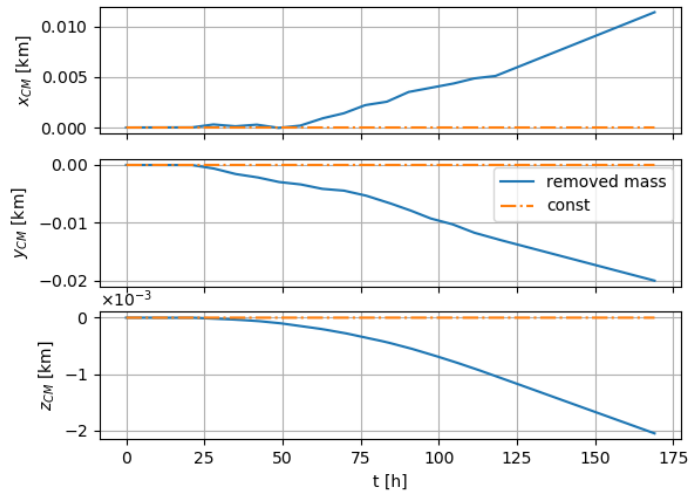

Figure 14: Itokawa center of mass position

Using the constant density polyhedron asteroid model described in [50] the gravitational environment on the surface of the asteroid can be computed. When combining the asteroid's gravitational attraction $\nabla U(\boldsymbol{r})$ on any point on its surface together with its rotation rate the geopotential state on the surface can be calculated. The acceleration vector at $\boldsymbol{r}$ in the rotating body-fixed frame is

$$\boldsymbol{r}'' = -\boldsymbol{\omega} \times (\boldsymbol{\omega} \times \boldsymbol{r}) - \dot{\boldsymbol{\omega}} \times \boldsymbol{r} + \nabla U(\boldsymbol{r}). \tag{7}$$

Figure 15 provides insight into the effective gravity acceleration over the surface of Itokawa. The nominal surface gravity field can be seen on the left. The change in the acceleration magnitude is shown on the right. It appears that the material removal clearly changed the structure and strength of the gravitational field.

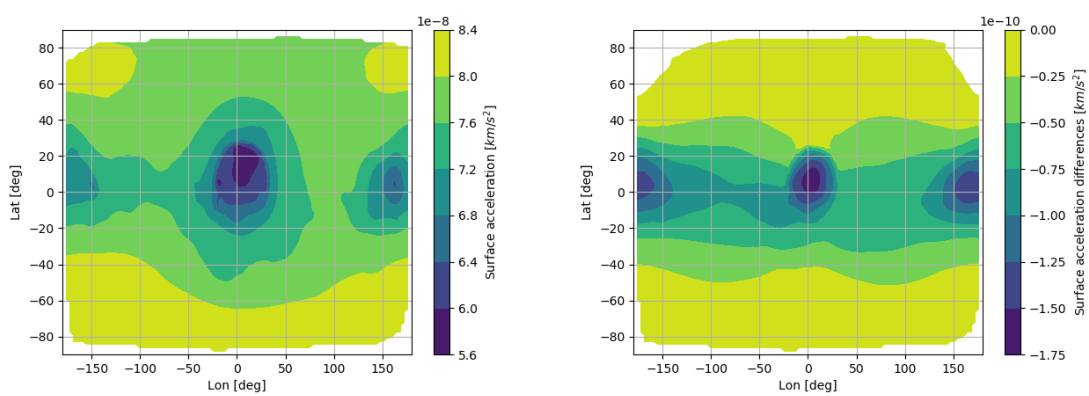

Figure 15: Itokawa's surface gravity field (left) and change in surface gravity magnitude (right) measured after material removal

Although this analysis is not comprehensive, it demonstrates that the rotational regime as well as the gravitational field of a rubble-pile asteroid subject to surface removal is susceptible to change over the course of an AoES mission. These must be taken into account while planning for AoES motion as well as surface material retrieval.

4 Mobility

Solar Radiation Pressure-enabled micro-gravity mobility is one of the key benefits of the AoES design, allowing the spacecraft to navigate about the small body of interest and perform precision landing in the vicinity of extractible material, without requiring any fuel or consumables besides the power delivered by the on-board RTGs. This section delves into the dynamics of the relative motion between the AoES and the asteroid, under the action of SRP. It is shown how SRP can be leveraged for the AoES' landing control and its potential in the post-hoping motion is demonstrated as well.

4.1 Deployment-Landing Sequence

4.1.1 Summary of findings

An abbreviated summary of this section's findings is provided below.

First of all, AoES are found to be able to land on small bodies from terminator orbits under the action of gravity and SRP, which allows the mothership that deploys the AoES to remain on a higher, safer orbit. An optimal control law was derived to lead the AoES to its targeted landing state. In addition, an approximate Time-Of-Flight between deployment and landing from a terminator orbit was obtained, which will help higher-level mission/system design. Under some simplifying assumptions, landing from a hyperbolic trajectory also appears feasible, a fact that will greatly ease mission design and provide more flexibility to mission planners.

These early-stage simulations could benefit from a number of extensions. As of now, the latitude of the landing point is arbitrary, but accurately targeting a low-latitude landing point would facilitate material retrieval after it has been thrown off of the asteroid. A significant milestone would also be to combine higher fidelity dynamics altogether with relative orbit determination, featuring a simulated communication channel with the mothership, while the AoES is subject to attitude maneuverability constraints. The impact dynamics also need to be investigated: the soft material the AoES is made of has an impact absorption capacity which needs to be accounted for while landing. In addition, the spacecraft design itself should probably be tailored to the targeted small body. For instance, the presence of outgassing and time-varying SRP due to elliptical heliocentric orbits would play a major role in choosing the AoES' area-to-mass ratio. Finally, the assumptions made in the hyperbolic landing case should be lifted so as to improve simulation realism. Another milestone would be to explore other orbits suitable for both the mothership and the AoES, and to investigate cooperative AoES deployment and operation.

4.1.2 Concept

AoES can control their orbit by leveraging the SRP force acting on their large surface made of soft material, in a way akin to solar sailing spacecraft. By actively exploiting SRP, a significant perturbation in small body proximity operation [41, 37], the spacecraft can achieve a variety of trajectories that are not possible for traditional small body landers such as Philae (Rosetta [4]) or MINERVA (Hayabusa [18]).

This unique capability brings greater flexibility to the typical AoES mission design, where a number of deployment-landing sequences take place, and therefore contributes to improving the mothership's safety as well.

Two promising deployment/landing scenarii under consideration are

1. AoES landing from a terminator orbit,
2. AoES landing from a hyperbolic trajectory.

These two options are achieved by the AoES while the mothership is safely 1) orbiting a stable orbit (such as a terminator orbit) or 2) passing by the target body on a flyby trajectory. In both cases, the mothership would never have to lower its altitude to near-landing levels.

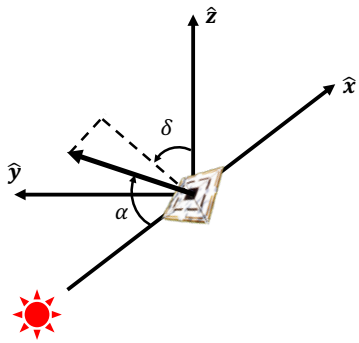

Figure 16: AoES attitude state

This fact is in remarkable contrast with traditional space missions featuring a landing component: for instance, the Hayabusa spacecraft descended close to the asteroid in order to deploy its lander payload [18], which arguably increased the mothership's risk of impact onto the body and as well as fuel consumption.

4.1.3 Optimal SRP landing from a terminator orbit

This section is concerned with the derivation of a landing control law under the assumption that the AoES is departing from a terminator orbit. In addition to the simulation results, an analytical derivation of the time of flight (ToF) upper bound is provided.

Coordinate frame and attitude definitions This paragraph introduces a few useful definitions for the derivations that follow. The coordinate frames of interest are the asteroid-centered rotating frame $\hat{x} - \hat{y} - \hat{z}$ and the LVLH orbit-fixed coordinate system $\hat{\boldsymbol{r}} - \hat{\boldsymbol{\theta}} - \hat{\boldsymbol{H}}$, both illustrated in Figure 17.

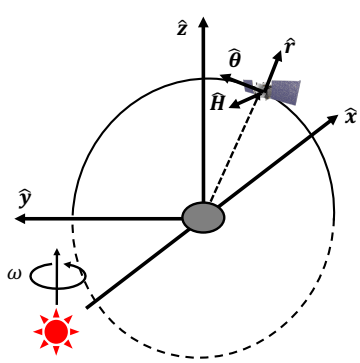

Figure 17: Local Vertical, Local Horizontal (LVLH) frame and asteroid-centered rotating frame

The spacecraft is modeled as a flat plate. Its attitude is defined as in Figure 16, where α is the pitch angle between the plate normal and the Sun-pointing direction and δ is the so-called clock angle. In this analysis, the control input vector is thus $\boldsymbol{u} = [\alpha, \delta]^T \in \mathcal{U} \subset \mathbb{R}^2$. For simplicity, let us assume that the reflectivity of the spacecraft surface is perfect up to a scaling parameter $\eta \in [0, 1]$. In the asteroid-centered rotating frame $\hat{x} - \hat{y} - \hat{z}$, the SRP acceleration $\boldsymbol{a}_{SRP_{xyz}} = [a_{SRP_x}, a_{SRP_y}, a_{SRP_z}]^T$ takes the following form:

$$\boldsymbol{a}_{SRP_{xyz}} = a_{SRP_0} \cos^2 \alpha \begin{bmatrix} \cos \alpha \\ -\sin \alpha \sin \delta \\ -\sin \alpha \cos \delta \end{bmatrix}, \tag{8}$$

where $a_{SRP_0} = (2\eta P_0 \sigma)/d^2$, d is the asteroid-sun distance, $P_0 \sim 1 \times 10^{17}[\mathrm{kg} \cdot \mathrm{m/s}^2]$ is the solar constant, and $\sigma[\mathrm{m}^2/\mathrm{kg}]$ is area/mass ratio. Representing the SRP acceleration in the LVLH frame yields:

$$\boldsymbol{a}_{SRP_{r\theta H}} = a_r \hat{\boldsymbol{r}} + a_\theta \hat{\boldsymbol{\theta}} + a_H \hat{\boldsymbol{H}}, \tag{9}$$

where a_r, a_θ, a_H are the components of the SRP acceleration along $\hat{\boldsymbol{r}}, \hat{\boldsymbol{H}}, \hat{\boldsymbol{\theta}}$ respectively. Hence,

$$\begin{bmatrix} a_r \\ a_\theta \\ a_H \end{bmatrix} \equiv \mathrm{Rot}_{A2O} \begin{bmatrix} a_{SRP_x} \\ a_{SRP_y} \\ a_{SRP_z} \end{bmatrix}, \tag{10}$$

where Rot_{A2O} represents the rotation matrix that converts a vector from the asteroid-centered frame into the orbit-fixed frame.

Dynamics For the sake of derivation simplicity, let us assume that the dominant forces acting on the spacecraft are the gravitational attraction of the small body and SRP. Under these assumptions, the dynamical system becomes the two body problem (small body and spacecraft) with SRP acceleration.

To deal with the dynamics, the Gauss form of Langrange's planetary equations are most suitable since the SRP force with attitude control is not a conservative force and thus cannot be expressed as a potential. Then the Gauss form of Lagrange's planetary equations are expressed as[49]

$$\begin{aligned}
\dot{a} &= \frac{2ha}{\mu(1-e^2)}(e \sin f a_r + (1 + e\cos f) a_\theta), \\
\dot{e} &= \left[\sin f a_r + \left(\frac{e + \cos f}{1 + e \cos f} + \cos f\right) a_\theta\right], \\
\dot{i} &= \frac{h}{\mu} \frac{\cos(\omega + f)}{1 + e\cos f} a_H, \\
\dot{\omega} &= \frac{h}{\mu}\left[-\frac{\cos f}{e} a_r + \frac{(2 + e\cos f)\sin f}{e(1 + e\cos f)} a_\theta - \frac{1}{\tan i}\frac{\sin(\omega + f)}{1 + e\cos f} a_H\right], \\
\dot{\Omega} &= \frac{h}{\mu \sin i}\frac{\sin(\omega + f)}{1 + e\cos f} a_H,
\end{aligned} \tag{11}$$

where $h = \sqrt{\mu a(1-e^2)}$ is the angular momentum of the spacecraft orbit, a, e, i, ω, Ω are the classical orbit elements.

These equations can be also written in the following matrix form:

$$\dot{\boldsymbol{x}} = \Xi_{r\theta H} \cdot \boldsymbol{a}_{SRP_{r\theta H}}, \tag{12}$$

where

$$\boldsymbol{x} \equiv \begin{bmatrix} a & e & i & \omega & \Omega \end{bmatrix}^T, \tag{13}$$

$$\Xi_{r\theta H} \equiv \begin{bmatrix} \boldsymbol{\xi}_{a_{r\theta H}} \\ \boldsymbol{\xi}_{e_{r\theta H}} \\ \boldsymbol{\xi}_{i_{r\theta H}} \\ \boldsymbol{\xi}_{\omega_{r\theta H}} \\ \boldsymbol{\xi}_{\Omega_{r\theta H}} \end{bmatrix} = \begin{bmatrix} \xi_{a_r} & \xi_{a_\theta} & \xi_{a_H} \\ \xi_{e_r} & \xi_{e_\theta} & \xi_{e_H} \\ \xi_{i_r} & \xi_{i_\theta} & \xi_{i_H} \\ \xi_{\omega_r} & \xi_{\omega_\theta} & \xi_{\omega_H} \\ \xi_{\Omega_r} & \xi_{\Omega_\theta} & \xi_{\Omega_H} \end{bmatrix} = \begin{bmatrix} \frac{2ha}{\mu(1-e^2)} e \sin f & \frac{2ha}{\mu(1-e^2)}(1 + e\cos f) & 0 \\ \frac{h}{\mu}\sin f & \frac{h}{\mu}\left(\frac{e+\cos f}{1+e\cos f} + \cos f\right) & 0 \\ 0 & 0 & \frac{h}{\mu}\frac{\cos(\omega+f)}{1+e\cos f} \\ -\frac{h}{\mu}\frac{\cos f}{e} & \frac{h}{\mu}\frac{(2+e\cos f)\sin f}{e(1+e\cos f)} & -\frac{h}{\mu\tan i}\frac{\sin(\omega+f)}{1+e\cos f} \\ 0 & 0 & \frac{h}{\mu\sin i}\frac{\sin(\omega+f)}{1+e\cos f} \end{bmatrix}. \tag{14}$$

Describing SRP acceleration in the orbit-fixed frame, the above equation is:

$$\dot{\boldsymbol{x}} = \Xi_{xyz} \cdot \boldsymbol{a}_{SRP_{xyz}}, \tag{15}$$

where

$$\Xi_{xyz} \equiv \begin{bmatrix} \boldsymbol{\xi}_{a_{xyz}} \\ \boldsymbol{\xi}_{e_{xyz}} \\ \boldsymbol{\xi}_{i_{xyz}} \\ \boldsymbol{\xi}_{\omega_{xyz}} \\ \boldsymbol{\xi}_{\Omega_{xyz}} \end{bmatrix} = \begin{bmatrix} \xi_{a_x} & \xi_{a_y} & \xi_{a_z} \\ \xi_{e_x} & \xi_{e_y} & \xi_{e_z} \\ \xi_{i_x} & \xi_{i_y} & \xi_{i_z} \\ \xi_{\omega_x} & \xi_{\omega_y} & \xi_{\omega_z} \\ \xi_{\Omega_x} & \xi_{\Omega_y} & \xi_{\Omega_z} \end{bmatrix} = \Xi_{r\theta H} \cdot [\mathrm{Rot}_{\mathrm{A2O}}]\,. \tag{16}$$

Attitude pitch angle constraint

Before proceeding with the control law derivation, we must be aware of the fact that, if the pitch angle is left unconstrained, the AoES will escape from the asteroid's sphere of influence. Terminator orbits arise from the balance of the gravitational attraction of a small body of interest and the SRP force; however the deployed terminator orbit is designed for the mothership, whose area/mass ratio is quite smaller than that of AoES. The pitch angle constraint is thus required to reduce the net SRP force affecting the AoES.

According to Scheeres (2012)[40] and Dankowicz (1994)[12], an energy-based argument leads to a simple upper-bound on the semi-major axis a_{max} that guarantees escape from the small body should the effective semi-major axis become larger:

$$a_{max} = \left(\frac{\mu}{\mu_{sun}}\right)^{1/3} \frac{\sqrt{3}d}{4\sqrt{\beta}},\ \beta = \frac{2\eta P_0 \sigma}{\mu_{sun}\epsilon},\ \epsilon = \left(\frac{\mu}{\mu_{sun}}\right)^{1/3} (<< 1), \tag{17}$$

where μ and μ_{sun} are the gravity parameters of the small body and the Sun.

Therefore, in order to ensure that no escape ensues for the entire orbit arc, the following constraint on the pitch angle $\alpha \geq \alpha_{min}$ must hold:

$$\alpha \geq \alpha_{min},\ \alpha_{min} = \arccos\left(\frac{1}{4}\sqrt{\frac{3\mu}{a_{SRP_0} a^2}}\right). \tag{18}$$

Orbit control law

For the dynamical system above, we derive a control law that drives an arbitrary set of orbital elements towards a desired one. We obtain a locally optimal feedback control law that exploits the properties of a so-called Lyapunov function.

Let an error vector of orbit elements be

$$\begin{aligned} &\delta\boldsymbol{x} \equiv \boldsymbol{x} - \boldsymbol{x}_r, \\ &\boldsymbol{x} \equiv \begin{bmatrix} a & e & i & \omega & \Omega \end{bmatrix}^T,\ \boldsymbol{x}_r \equiv \begin{bmatrix} a_r & e_r & i_r & \omega_r & \Omega_r \end{bmatrix}^T, \end{aligned} \tag{19}$$

where $\boldsymbol{x}_r$ is a set of reference orbit elements that we want to reach. Then, with a weight matrix $P \in \mathbb{R}^{n\times n}$ (n: number of elements in $\boldsymbol{x}$), an optimal feedback control input $\boldsymbol{u}_{FB}$ is

$$\begin{aligned} J =& \frac{dV}{dt},\ V = \frac{1}{2}\delta\boldsymbol{x}^T \cdot P \cdot \delta\boldsymbol{x}, \\ \boldsymbol{u}_{FB} =& \arg\min_{\boldsymbol{u}\in\mathcal{U}} J = \arg\min_{\boldsymbol{u}\in\mathcal{U}} \delta\boldsymbol{x}^T \cdot P \cdot \dot{\boldsymbol{x}} = \arg\min_{\boldsymbol{u}\in\mathcal{U}} \delta\boldsymbol{\xi}_{xyz}^T \cdot \boldsymbol{a}_{SRP_{xyz}}, \end{aligned} \tag{20}$$

where $\delta\boldsymbol{\xi}_{xyz}^T = \delta\boldsymbol{x}^T \cdot P \cdot \Xi_{xyz} (\in \mathbb{R}^{3\times 1})$. The weight matrix P represents how the designer aims to control the orbit. For instance, setting $P = \mathrm{diag}[1, 1, 1, 0, 1]$ would control $\{a, e, i, \Omega\}$ with the same weight.

Since $\delta\boldsymbol{\xi}_{xyz}$ is independent from the control variables, $\boldsymbol{u}_{FB}$ satisfies the following equations

$$\begin{aligned}
\mathcal{J}(\boldsymbol{u}_{FB}) &= \left.\frac{\partial(\delta\boldsymbol{\xi}_{xyz}^T \cdot \boldsymbol{a}_{SRP_{xyz}})}{\partial \boldsymbol{u}}\right|_{\boldsymbol{u}_{FB}} \\
&= a_{SRP_0}\ \delta\boldsymbol{\xi}_{xyz}^T \begin{bmatrix} -3\cos^2\alpha\sin\alpha & 0 \\ -\cos\alpha\sin\delta(1-3\sin^2\alpha) & -\cos^2\alpha\sin\alpha\cos\delta \\ -\cos\alpha\cos\delta(1-3\sin^2\alpha) & \cos^2\alpha\sin\alpha\sin\delta \end{bmatrix}_{\boldsymbol{u}_{FB}} \\
&= \mathbf{0}_{1\times 2}, \qquad (21) \\
\det[\mathcal{H}(\boldsymbol{u}_{FB})] &= \det[a_{SRP_0}\ \delta\boldsymbol{\xi}_{xyz}^T \mathscr{A}_{ijk}]_{\boldsymbol{u}_{FB}} > 0, \qquad (22)
\end{aligned}$$

where Equation (8) is used and $\mathscr{A}_{ijk}$ is a 3-rank tensor of $\mathbb{R}^{2\times2\times3}$ defined as

$$\mathscr{A}_{ijk} = \frac{\partial^2 a_{SRP_k}}{\partial i\ \partial j}. \qquad (23)$$

This equation can be analyticaly solved and yields

$$\begin{aligned}
\delta_{FB} &= \arctan\left(\frac{\delta\xi_y}{\delta\xi_z}\right),\ \operatorname{sign}(\cos\delta) = \operatorname{sign}(\delta\xi_z) \\
\alpha_{FB} &= \frac{1}{2}\arccos\left[\frac{1}{3}\left(1-\gamma_x^2-\gamma_x\sqrt{\gamma_x^2+8}\right)\right],
\end{aligned} \qquad (24)$$

where

$$\gamma_x \equiv \delta\xi_x/\delta\xi = \delta\xi_x/\sqrt{\delta\xi_x^2+\delta\xi_y^2+\delta\xi_z^2}, \qquad (25)$$

The trivial solution $\alpha = 0$ is excluded since it represents no control and is of no interest. Representing the optimal value in the pitch angle constraint by using the superscript §, the control input vector with the constraint is described as

$$\boldsymbol{u}_{FB}^{\S} = [\alpha_{FB}^{\S}, \delta_{FB}],\ \alpha_{FB}^{\S} = \max[\alpha_{FB}, \alpha_{min}]. \qquad (26)$$

Upper bound of ToF

The upper bound of the Time of Flight (ToF) is a valuable piece of information for mission designers, since the solution space is too large to permit trial-and-error design. With some approximation, we can analytically derive a upper bound of ToF expressed in terms of the design parameters. The resultant ToF_{ub} formulation is

$$\begin{aligned}
ToF_{ub} =& ToF_{ub}^{\S}(a_0, a_b) + ToF_{ub}^{*}(a_b, a_f) = \frac{2}{3C_1}\left(a_b^{3/2} - a_0^{3/2}\right) + \frac{2}{C_2}\left(a_b^{-1/2} - a_f^{-1/2}\right), \\
a_b =& \frac{9\mu}{32 a_{SRP_0}},\ C_1 = -\frac{3}{8}\sin\alpha^{\#}\sqrt{\mu},\ C_2 = -\frac{2a_{SRP_0}}{\sqrt{\mu}}\cos^2\alpha^{\#}\sin\alpha^{\#},\ \alpha^{\#} = \frac{1}{2}\arccos\frac{1}{3},
\end{aligned} \qquad (27)$$

where a_b is the border where the pitch angle constraint switches from active to inactive. Figure 18 illustrates the ToF_{ub} when landing on Bennu and Itokawa. Additionaly, Figure 19 shows simulated values of the ToF from numerical propagations of the trajectories driven by the control low derived above, which confirm that the upper bound formulation actually is a good approximation.

One of the most important piece of information one could get from these figures is the answer to *"how large the area/mass ratio value should be in order to achieve a mission scenario goal."* For instance, in a case where it is required to land the AoES from a 1 km altitude termiinator orbit on asteroid Bennu within 5 days (a choice that could be motivated by various reasons, such as battery capacity,...), the area/mass ratio σ should be larger than 0.1 m^2/kg. Time-variation of the asteroid-sun distance is the reason why each

region corresponding to a certain value of σ has a varying width in the $x-$axis. These figures clearly indicate how the ToF is affected by each design factor including the deployment altitude (a measure of how safe the mothership is), target asteroid (gravity field, solar distance, and size), and area/mass ratio.

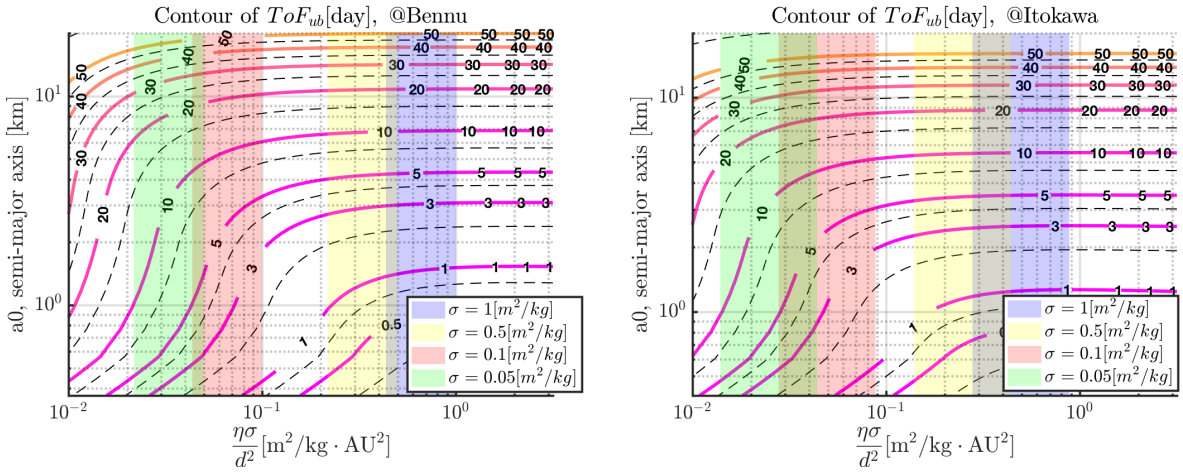

Figure 18: Upper bound of the ToF [day].

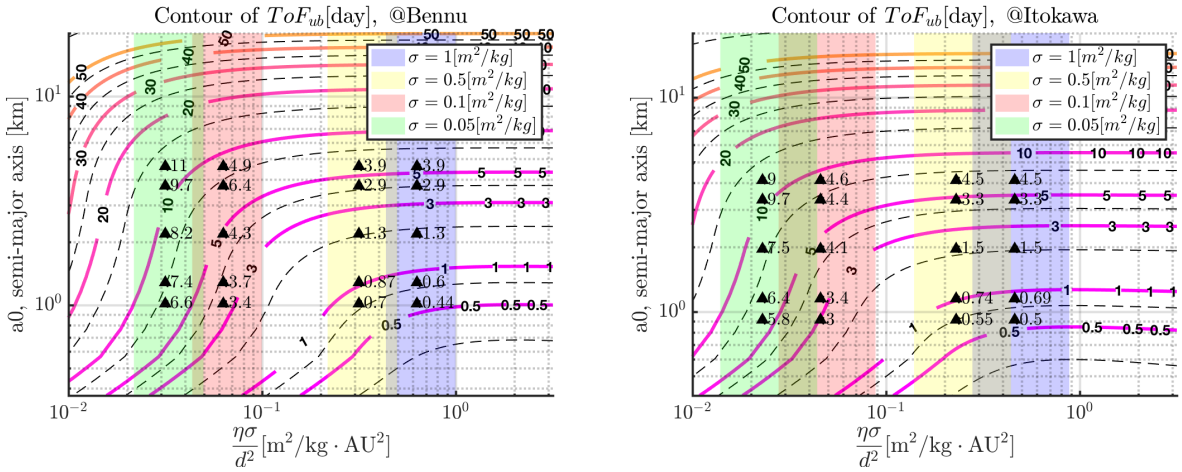

Figure 19: Upper bound of the ToF [day]. Values of the ToF obtained by numerical simulation are plotted with black diamonds.

Simulation results

This section illustrates the capability of the derived control law with some representative nominal landing trajectories, along with those featuring error sources (control error on attitude and knowledge error on spacecraft position and velocity). In this section, the AoES specification is assumed as area/mass ratio $\sigma = 0.5$ m^2/kg and reflection coefficient $\eta = 0.8$. Also, for asteroid parameters, the following values are used: the gravity parameter $\mu_{Bennu} = 4.0 \times 10^{-9}$ km^3/s^2, $\mu_{Itokawa} = 2.1 \times 10^{-9}$ km^3/s^2 and the solar distance $d_{Bennu} = 1.1264$ AU, $d_{Itokawa} = 1.3241$ AU.

Nominal trajectories

Some examples of simulation results are shown in Figure 20. The left figure shows a landing trajectory

generated by semi-major axis reduction control, and the right one shows a trajectory with inclination change control. The figures also illustrate the terminator orbit where AoES is deployed and where the mothership remains.

As can be expected, the semi-major axis reduction control results in a fast, straight landing trajectory, the inclination change control enables the AoES to land at lower latitudes, which would be beneficial for retrieving the mass that is removed from the surface.

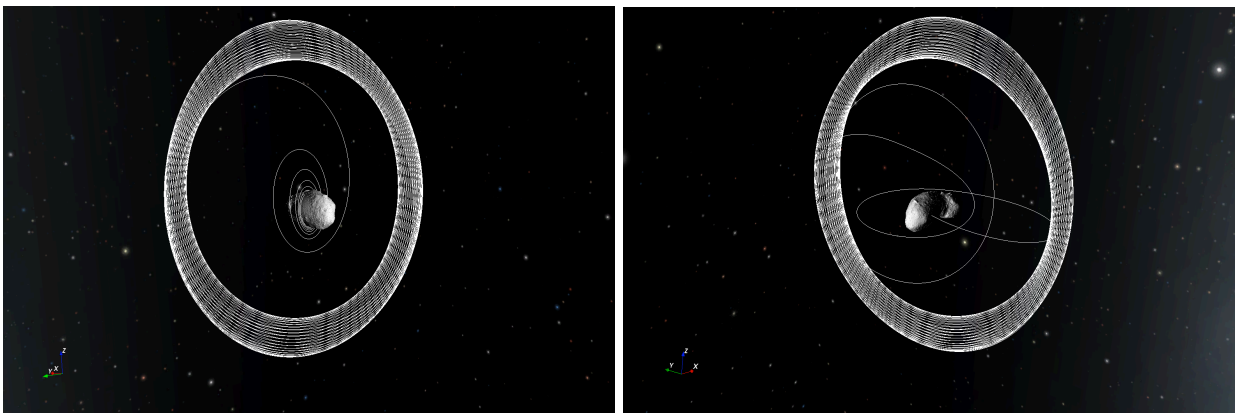

Figure 20: AoES @ Itokawa, landing from a terminator orbit. Left: reducing semi major axis; right: changing inclination.

Orbit control results with error

This section qualitatively confirms the validity of the control law, as shown by the simulation results that incorporate some errors sources.

Before adding any error to the position and velocity components, we should be aware of the escape velocity of the orbited body at a specific altitude, in order to make sure that the spacecraft escape due to too large of an error in the velocity or position components. The escape velocity around a point-mass primary body is

$$v_{esc} = \sqrt{\frac{2\mu}{r}}, \tag{28}$$

hence the escape velocities around Bennu and Itokawa at 1.5 [km] altitude, an altitude close to that of the nominal terminator orbit of the OSIRIS-REx spacecraft, are $v_{esc_{\text{bennu}}} = 7.30$ [cm/s] and $v_{esc_{\text{itokawa}}} = 5.29$ [cm/s]. From this, error sources used in the simulation are assumed as attitude control error $\sigma_{att} = 3$ [deg] and position and velocity knowledge errors $\sigma_{pos} = 5$ [m], $\sigma_{vel} = 1.5$ [cm/s].

Some trajectories with these errors are displayed in Figure 21. This figure includes 20 landing trajectories where the control law of reducing semi-major axis is employed. As can be seen, the control law generates trajectories that are consistent with the nominal one and their respective errors.

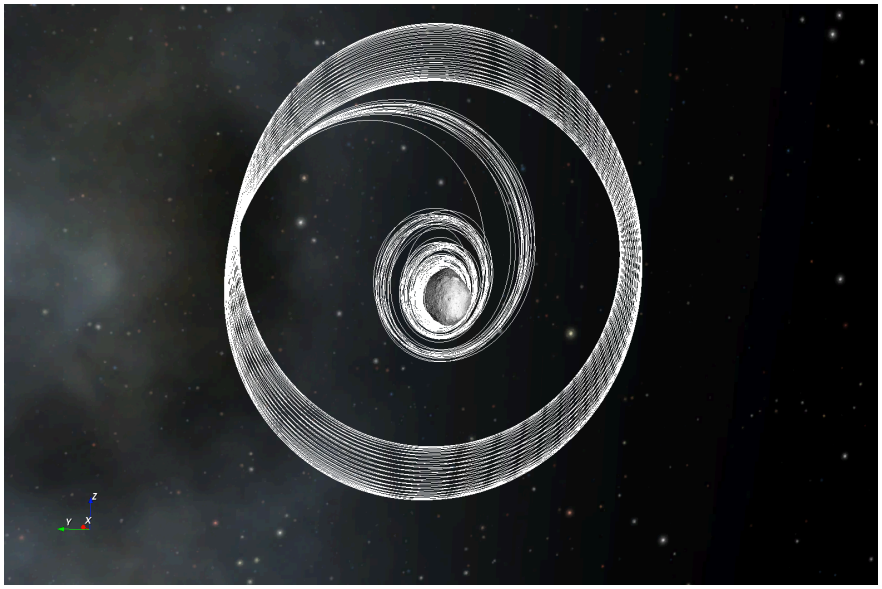

Figure 21: Monte-Carlo results featuring 20 AoES trajectory @ Itokawa, landing from a terminator orbit, with error added to the initial attitude, position and velocity components. The control law was reducing the semi-major axis only

4.1.4 Landing from a hyperbolic trajectory

This section analytically discusses the capability and limitation of landing from hyperbolic trajectories.

For the sake of the discussion, we assume simplified dynamics where

- both the target small body and spacecraft move in the ecliptic plane (2-D motion),
- the gravitational forces due to the targeted small body is negligible.

A conceptual depiction of this sequence and the definition of all parameters are shown in Figure 22. The mothership is on a trajectory that flybys the targeted small body at the relative speed V_∞ with an impact parameter h_∞ and deploys the AoES at a distance y_0 before the closest approach. The AoES controls its trajectory by using SRP through its only attitude control α, which is defined as in the figure, targeting the center of the target body. The origin is at the center of the target body.

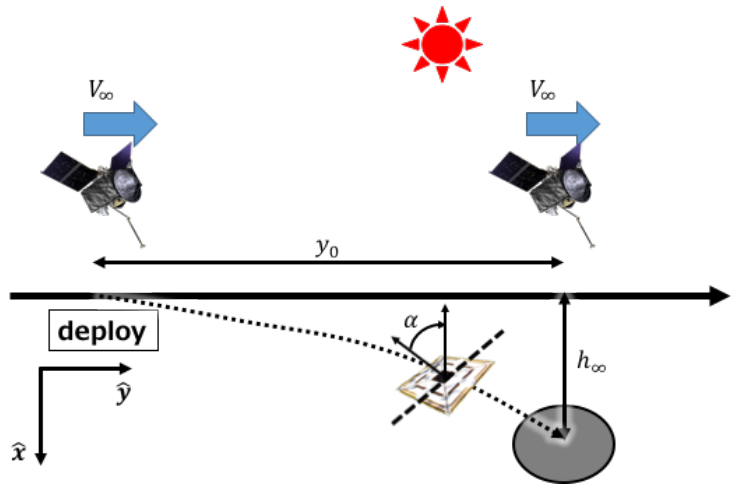

Figure 22: Concept illustration of landing from a hyperbolic orbit.

The acceleration acting on the spacecraft, which is only due to SRP in this case, is expressed as

$$\begin{aligned} \ddot{x} =& a_{SRP0} \cos^3 \alpha, \\ \ddot{y} =& - a_{SRP0} \cos^2 \alpha \sin \alpha, \\ h_{max} =& \frac{1}{2} a_{SRP0} \left(\frac{y_0}{V_\infty} \right)^2. \end{aligned} \tag{29}$$

In the case where the spacecraft attitude with respect to the Sun is fixed to a constant value α_0,

$$\begin{aligned} x =& - h_\infty + \frac{1}{2} a_{SRP0} \cos^3 \alpha_0 \ t^2, \\ y =& - y_0 + V_\infty t - \frac{1}{2} a_{SRP0} \cos^2 \alpha_0 \sin \alpha_0 \ t^2. \end{aligned} \tag{30}$$

For landing, $x = y = 0$ at $t = t_f$, hence

$$\begin{aligned} 0 =& - h_\infty + \frac{1}{2} a_{SRP0} \cos^3 \alpha_0 \ t_f^2, \\ 0 =& - y_0 + V_\infty t_f - \frac{1}{2} a_{SRP0} \cos^2 \alpha_0 \sin \alpha_0 \ t_f^2, \end{aligned} \tag{31}$$

which result in

$$\begin{aligned} t_f =& \sqrt{\frac{2 h_\infty}{a_{SRP0} \cos^3 \alpha}}, \\ \alpha_0 =& \arg \left[\cos^3 \alpha_0 \left(\frac{y_0}{h_\infty} + \tan \alpha_0 \right)^2 - \frac{2 V_\infty^2}{a_{SRP0} h_\infty} = 0 \right]. \end{aligned} \tag{32}$$

Given the mother's flyby speed V_∞, closest approach distance h_∞, and deployment position y_0, numerically solving this equation yields the fixed attitude control parameter α_0 amd ToF t_f. We can then compute the landing speed V_{ref_f}, the AoES' relative speed with respect to the body. Contour plots of the landing speed V_{rel_f} with respect to various V_∞, h_∞, and y_0 are shown in Figure 23, 24, and 25. The assumed parameters are similar to the values used by Takahashi and Scheeres [47]. In these plots, regions where the landing is impossible are colored in white.

We see that AoES have a certain control authority to successfully achieve the hyperbolic landing for some flyby conditions while the landing speed is basically almost the same as the original speed, that is to say, the flyby speed. As an example, AoES would be able to land from a flyby trajectory of $h_\infty = 2$ km and $V_\infty = 5$ m/s if deployed at a distance $y_0 = 300$ km . For the sake of mission design, the maximum allowable closest approach distance h_∞ with respect to the flyby speed V_∞ and the deployment position y_0 is shown in Figure 26. Note that the contour value is expressed in log scale.

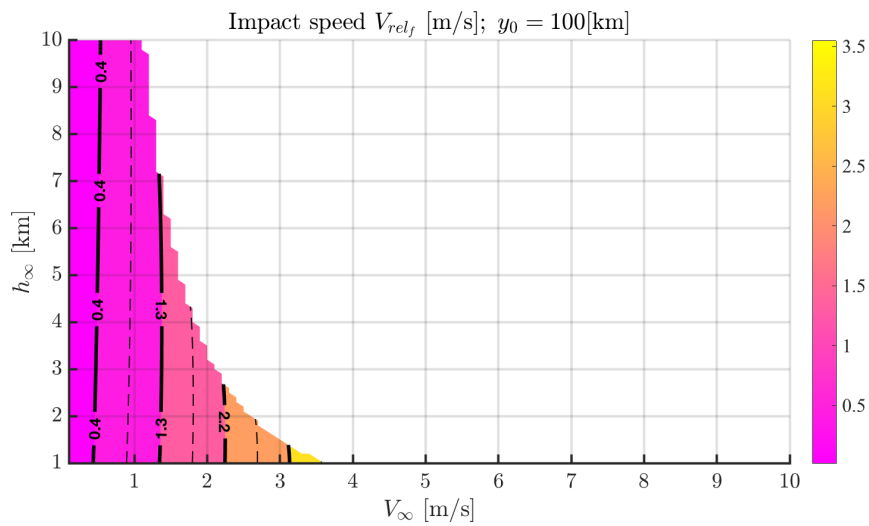

Figure 23: Impact speed V_{rel_f} with respect to V_∞ and h_∞.

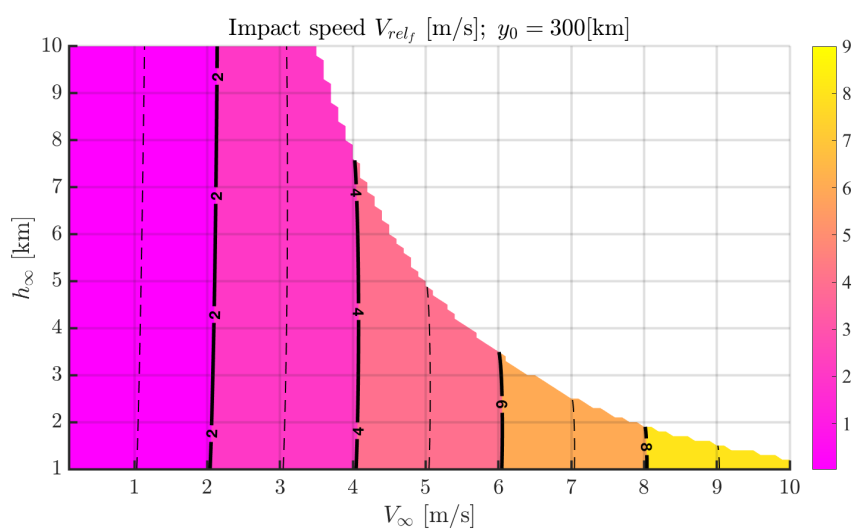

Figure 24: Impact speed V_{rel_f} with respect to V_∞ and h_∞.

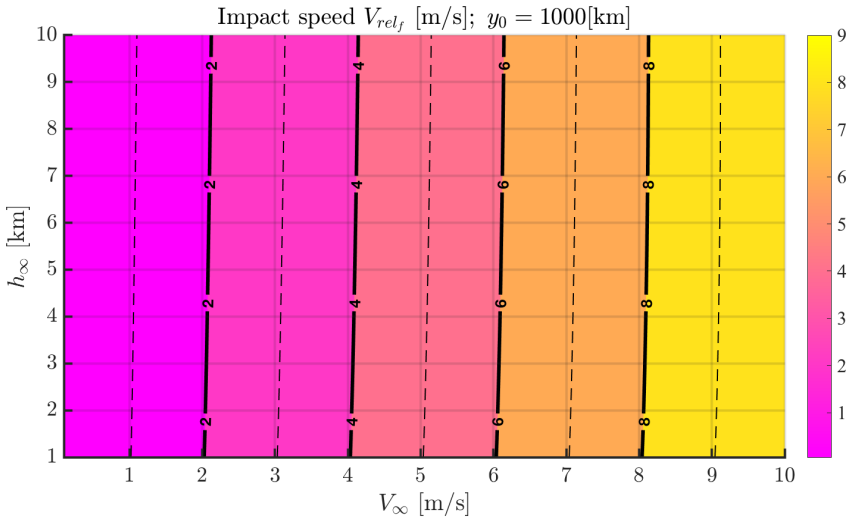

Figure 25: Impact speed V_{rel_f} with respect to V_∞ and h_∞.

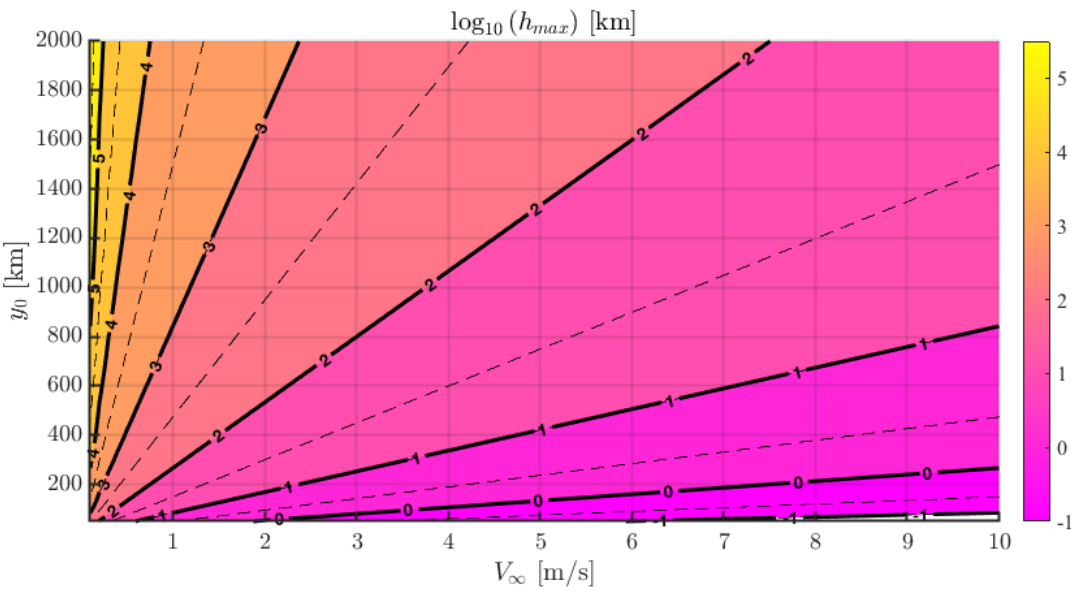

Figure 26: Maximum h_∞ allowable for landing with respect to V_∞ and y_0.

In conclusion, we have demonstrated that SRP can be leveraged to land on the surface of an asteroid under some assumptions. Future work avenues are as listed on page 15, and should greatly improve the fidelity of the landing simulations once implemented.

4.2 Lift-off from asteroid surface due to SRP

This section aims at quantifing how much of an effect SRP could have on an object landed on the surface of the small body of interest. In this study, the landed object is taken as a wedge identical to the one shown on Figure 27.

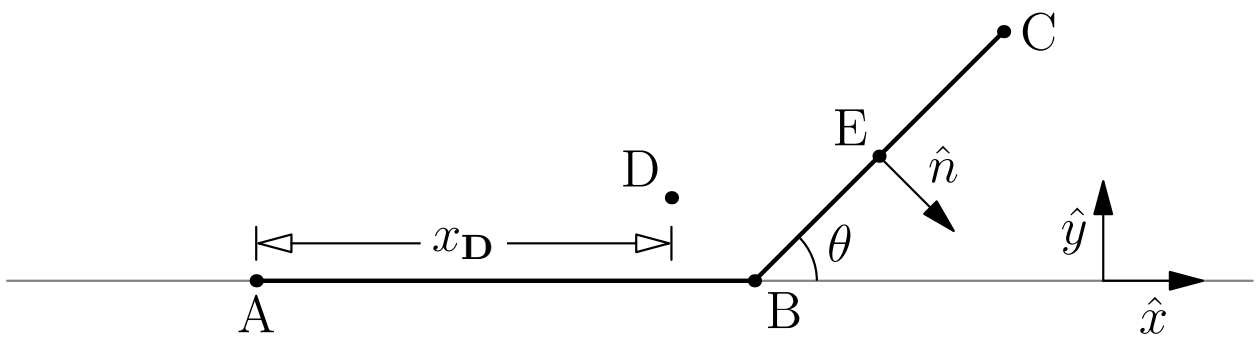

Figure 27: Geometry of the lift-off problem

The surface element **ABC** is a rigid object comprised of two segments: **AB** and BC. **AB** is aligned with the surface of the asteroid. **BC** is at a constant angle θ from **AB**.

From basic geometry, we have

$$\mathbf{AB} = l\hat{x} \tag{33}$$

$$\mathbf{BC} = L\left(\hat{y}\sin\theta + \hat{x}\cos\theta\right) \tag{34}$$

A plate model as proposed in [14] is retained to represent the SRP force

$$\mathbf{F}_{SRP} = -\frac{\Phi A}{c}\sin\theta\left(2\left[\frac{\delta}{3} + \rho\sin\theta\right]\hat{n} + (1-\rho)\,\hat{x}\right) \tag{35}$$

where Φ is the solar flux at the asteroid, $A = Ld$ the surface area of the **BC** side, ρ the specular reflectivity and δ the diffuse reflectivity. $\hat{n}$ is the sun-facing plate normal with $\hat{x}$ being the sun-pointing direction. The wedge **ABC** has a constant depth d and a constant area to mass ratio $\sigma = \frac{(l+L)d}{m}$.

Hypothetical adhesive forces are assumed to have a constant distribution f across **AB**, adding up to a total force

$$\mathbf{F}_{\text{adhesion}} = -F\hat{y} = -fdl\hat{y} \tag{36}$$

Finally, **ABC** is subject to gravity as in

$$\mathbf{F}_{\text{gravity}} = m\mathbf{g} \tag{37}$$

where $\mathbf{g}$ is directed along $-\hat{y}$ and of magnitude $\|\mathbf{g}\| = \frac{\mu}{R^2} - \omega^2 R$, where μ and R stand for the asteroid's standard gravitational parameter and asteroid's radius.

4.2.1 Derivation of translating lift-off conditions

Translating lift-off can occur if the $\hat{y}$ component of the sum of external forces $\mathbf{F}$ acting on **ABC** is positive. We have

$$\mathbf{F} = \mathbf{F}_{\text{gravity}} + \mathbf{F}_{\text{SRM}} + \mathbf{F}_{\text{adhesion}} \tag{38}$$

with

$$\mathbf{F}_{\text{gravity}} = m\mathbf{g} = -\frac{(l+L)\,d}{\sigma}g\hat{y} \tag{39}$$

$$\mathbf{F}_{\text{SRP}} = -\frac{\Phi A}{c}\sin\theta\left(2\left[\frac{\delta}{3} + \rho\sin\theta\right]\hat{n} + (1-\rho)\,\hat{x}\right) \tag{40}$$

$$\mathbf{F}_{\text{SRP}} = -F\hat{y} \tag{41}$$

So the $\hat{y}$ component of these forces reads

$$\boxed{\mathbf{F}^T\hat{y} = -\frac{(l+L)\,d}{\sigma}g + \frac{2\Phi Ld}{c}\sin\theta\left[\frac{\delta}{3} + \rho\sin\theta\right]\cos\theta - fld} \tag{42}$$

4.2.2 Derivation of pivoting lift-off conditions

The lift-off conditions can be determined by computing the sum of the moments induced by all forces about **A**. We have

$$\boldsymbol{\mathcal{M}}_A = \boldsymbol{\mathcal{M}}_{\mathbf{A},\text{adhesion}} + \boldsymbol{\mathcal{M}}_{\mathbf{A},\text{gravity}} + \boldsymbol{\mathcal{M}}_{\mathbf{A},\mathbf{SRP}} \tag{43}$$

Lift-off may ensue only if the component of $\boldsymbol{\mathcal{M}}_A$ along $\hat{z} = \hat{x} \times \hat{y}$ is positive.

Derivation of $\boldsymbol{\mathcal{M}}_{\mathbf{A},\text{gravity}}$ The moment created by gravity at **A** reads

$$\boldsymbol{\mathcal{M}}_{\mathbf{A},\text{gravity}} = \boldsymbol{\mathcal{M}}_{\mathbf{D},\text{gravity}} + \mathbf{AD} \times (m\mathbf{g}) \tag{44}$$

$$= m\left(\mathbf{AD} \times \mathbf{g}\right) \tag{45}$$

Writing out and expanding the definition of the center-of-gravity **D**

$$\boldsymbol{\mathcal{M}}_{\mathbf{D},\text{gravity}} = \mathbf{0} \tag{46}$$

we find

$$\hat{x}^T \mathbf{AD} = x_{\mathbf{D}} = \frac{1}{l+L}\left(\frac{l^2}{2} + lL + \frac{L^2}{2}\cos\theta\right) \tag{47}$$

so

$$\boxed{\boldsymbol{\mathcal{M}}_{\mathbf{A},\text{gravity}} = -\frac{mg}{l+L}\left(\frac{l^2}{2} + lL + \frac{L^2}{2}\cos\theta\right)\hat{z}} \tag{48}$$

Derivation $\boldsymbol{\mathcal{M}}_{\mathbf{A},\mathbf{SRP}}$ The total force created by SRP is

$$\mathbf{F}_{SRP} = -\frac{\Phi A}{c}\sin\theta\left(2\left[\frac{\delta}{3} + \rho\sin\theta\right]\hat{n} + (1-\rho)\,\hat{x}\right) \tag{49}$$

Since the SRP force distribution is constant across **BC**, it is clear that

$$\boldsymbol{\mathcal{M}}_{\mathbf{E},\mathbf{SRP}} = \mathbf{0} \tag{50}$$

Hence

$$\boldsymbol{\mathcal{M}}_{\mathbf{A},\mathbf{SRP}} = \boldsymbol{\mathcal{M}}_{\mathbf{E},\mathbf{SRP}} + \mathbf{AE} \times \mathbf{F}_{SRP} \tag{51}$$

$$= \mathbf{AE} \times \mathbf{F}_{SRP} \tag{52}$$

$$= -\left(l\hat{x} + \frac{L}{2}\left(\hat{y}\sin\theta + \hat{x}\cos\theta\right)\right) \times \frac{\Phi A}{c}\sin\theta\left(2\left[\frac{\delta}{3} + \rho\sin\theta\right]\hat{n} + (1-\rho)\,\hat{x}\right) \tag{53}$$

$$= -\frac{\Phi A}{c}\sin\theta\left(\left[\frac{\delta}{3} + \rho\sin\theta\right]\left[2l\left(\hat{x}\times\hat{n}\right) + L\left(\hat{y}\sin\theta + \hat{x}\cos\theta\right)\times\hat{n}\right] + \frac{L\sin\theta\,(1-\rho)}{2}\left(\hat{y}\times\hat{x}\right)\right) \tag{54}$$

$$= -\frac{\Phi A}{c}\sin\theta\left(\left[\frac{\delta}{3} + \rho\sin\theta\right]\left[-2l\cos\theta\hat{z} + L\left(-\hat{z}\sin^2\theta - \hat{z}\cos^2\theta\right)\right] - \frac{L\sin\theta\,(1-\rho)}{2}\hat{z}\right) \tag{55}$$

$$= \frac{\Phi A}{c}\sin\theta\left(\left[\frac{\delta}{3} + \rho\sin\theta\right]\left[2l\cos\theta + L\right] + \frac{L\sin\theta\,(1-\rho)}{2}\right)\hat{z} \tag{56}$$

Hence

$$\boxed{\boldsymbol{\mathcal{M}}_{\mathbf{A},\mathbf{SRP}} = \frac{\Phi A}{c}\sin\theta\left(\left[\frac{\delta}{3} + \rho\sin\theta\right]\left[2l\cos\theta + L\right] + \frac{L\sin\theta\,(1-\rho)}{2}\right)\hat{z}} \tag{57}$$

Derivation of $\boldsymbol{\mathcal{M}}_{\mathbf{A},\text{adhesion}}$ Since the adhesive forces have a constant distribution across **AB**, adding up to a total force $\mathbf{F}_{\text{adhesion}} = -F\hat{y} = -fld\hat{y}$, it is straightforward to get

$$\boxed{\boldsymbol{\mathcal{M}}_{\mathbf{A},\text{adhesion}} = -\frac{l}{2}F\hat{z}} \tag{58}$$

Lift-off can ensue if the following equation is satisfied

$$\boldsymbol{\mathcal{M}}_A^T\hat{z} \geq 0 \tag{59}$$

or

$$\boxed{\boldsymbol{\mathcal{M}}_A^T\hat{z} = -\frac{gd}{\sigma}\left(\frac{l^2}{2} + lL + \frac{L^2}{2}\cos\theta\right) + \frac{\Phi Ld}{c}\sin\theta\left(\left[\frac{\delta}{3} + \rho\sin\theta\right][2l\cos\theta + L] + \frac{L\sin\theta\,(1-\rho)}{2}\right) - \frac{l^2}{2}fd} \tag{60}$$

4.2.3 Numerical example

It is clear that for vertical take-off to ensue, the SRP force acting on **BC** must be greater than the weight of this segment. This must be the case regardless of the adhesion forces acting on **AB**. In what follows, an area-to-mass ratio of $\sigma = 0.5$ m^2/kg is assumed. The asteroid is taken as a rubble-pile of constant density $\rho = 1000$ kg/m^3. The resulting g factors in the point-mass acceleration caused by the mass concentration and the opposite effect due to the asteroid rotation. The specular reflectivity of **BC** was set to $\rho = 1$ and its diffusive component to $\delta = 0$. The material the wedge is made of is thus akin to a perfectly white, regular surface.

The magnitude of the force-per-unit-length $\frac{\mathbf{F}^T\hat{y}}{d}$ caused by gravity and SRP over **BC** are compared on Figure 28. Fast rotation appears to be a *sine-qua-non* condition for SRP to possibly overtake gravity. The force-per-length positive excess does not exceed the μN/m range. Adding adhesion over **AB** would overcome this potential force excess and keep the wedge connected with the ground.

Pivotal take-off about **A** can also be investigated. To this end, the moment-per-unit-length $\frac{\boldsymbol{\mathcal{M}}_A^T\hat{z}}{d}$ of SRP and gravity over **ABC** is plotted on Figure 29. The asymptotic decrease of the gravity torque is due to the displacement of the center of gravity **D** as θ increases. The asymptote lines up with the angle yielding $x_{\mathbf{A}} = x_{\mathbf{D}} = 0$. Unsurprisingly, the critical angle approaches $\frac{\pi}{2}$ as L increases. Because the torque cause by gravity about **A** vanishes in this critical configuration, there are no other torques to oppose the effect of SRP and rotational motion becomes possible, although at a slow rate.

In both cases, the excess in force or torque inducing movement off the surface is at best minuscule, at worse completely superseded by gravity, let alone adhesion. This analysis did not cover the whole range of asteroids or lander configurations, but provided insight into the significant figures of the problem at and below $\sigma = 0.5$ m^2/kg.

In conclusion, translational or pivotal take-off of the wedge **ABC** appears unlikely given non-zero amounts of adhesive forces, although a combination of a small, fast-spinning asteroid close to the sun could facilitate departure if an impulse severing the adhesive link is provided. This is the scenario investigated in the next section.

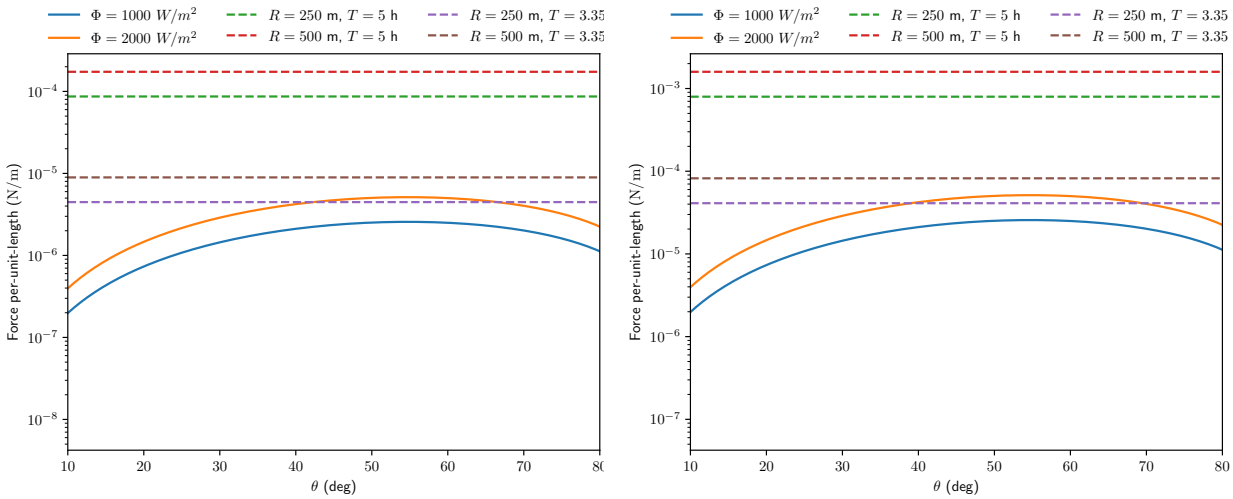

Figure 28: Magnitude of the SRP (bold) and gravity (dashed) force-per-unit-length with $l = 0.1$ m, $L = 1$ m (left) and $l = 0.1$ m, $L = 10$ m (right) for varying asteroid sizes, spin rates and solar fluxes.

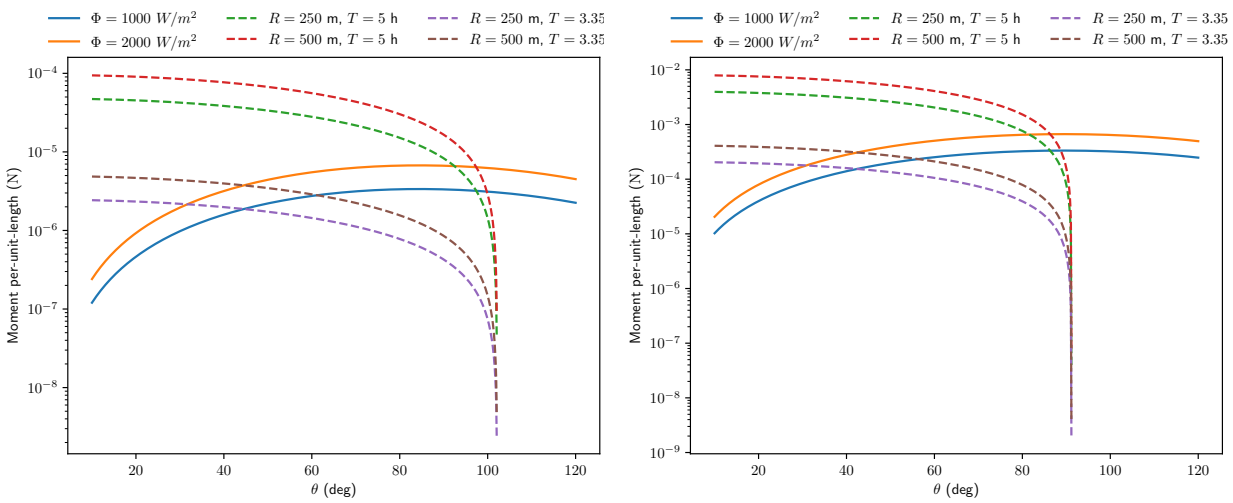

Figure 29: Magnitude of the SRP (bold) and gravity (dashed) moment-per-unit-length with $l = 0.1$ m, $L = 1$ m (left) and $l = 0.1$ m, $L = 10$ m (right) for varying asteroid sizes, spin rates and solar fluxes.

4.3 Lift-off trajectory under the action of SRP

4.3.1 Dynamics

The previous section has demonstrated that SRP should not be sufficient to scoop an object off the surface of a small body. However, the situation would change should a small impulse be imparted to the object. This section investigates such a case, in a simplfied scenario. The object is now a plate of area-to-mass ratio $\sigma = 0.5$ m^2/kg, and is initially located at the equator of the small body. Furthermore, the plate maintains a constant pitch angle between its normal vector $\hat{n}$ and the asteroid-to-sun direction $\hat{s}$.

The small body is an asteroid undergoing principal-axis rotation at an angular velocity

$$\boldsymbol{\omega} = \begin{pmatrix} 0 \\ 0 \\ \omega \end{pmatrix}^{\mathcal{N}} \tag{61}$$

with ω constant. The direction cosine matrix $[\mathcal{BN}]$ denoting a coordinate transformation from $\mathcal{N}$ to the asteroid body-fixed frame $\mathcal{B}$ reduces to an elemental rotation matrix about the third inertial axis:

$$[\mathcal{BN}](t) = \begin{bmatrix} \cos\omega t & \sin\omega t & 0 \\ -\sin\omega t & \cos\omega t & 0 \\ 0 & 0 & 1 \end{bmatrix} \tag{62}$$

The asteroid itself is taken as a spheroid of radius R and constant density ρ. The asteroid-to-sun direction is inertially constant and equal to

$$\hat{s} = \begin{pmatrix} 1 \\ 0 \\ 0 \end{pmatrix}^{\mathcal{N}} \tag{63}$$

The dynamics acting on the plate in the asteroid-fixed reference frame are given by

$$\mathbf{r}'' = -\frac{\mu}{r^3}\mathbf{r} + \frac{1}{m}\mathbf{F}_{SRP} - 2\boldsymbol{\omega} \times \mathbf{r}' - \boldsymbol{\omega} \times \boldsymbol{\omega} \times \mathbf{r} \tag{64}$$

where we are still using the same plate model as Gobinddas et al [14].

$$\mathbf{F}_{SRP} = -\frac{\Phi A}{c}\sin\theta\left(2\left[\frac{\delta}{3} + \rho\sin\theta\right]\hat{n} + (1-\rho)\,\hat{s}\right) \tag{65}$$

with $\mathbf{r}$, $\mathbf{r}'$ and $\mathbf{r}''$ being the position, velocity and acceleration as seen in the rotating frame of the asteroid. The area-to-mass ratio is denoted $\sigma = \frac{A}{m}$. The attitude of the plate is enforced to a sun pointing attitude: $\hat{n} \equiv \hat{s}$. This corresponds to setting $\theta = \frac{\pi}{2}$ in the above equation.

The goal of this study is to investigate the joint effect of an initial body-frame velocity $\mathbf{r}_0'$ of magnitude v and SRP on the plate's trajectory. Random samples of $\mathbf{r}_0'$ were generated like so:

1. A random vector $\mathbf{d}$ was sampled from a three-dimensional standard Gaussian distribution.
2. A random direction $\hat{d}$ was extracted from $\hat{d} = \frac{\mathbf{d}}{\|\mathbf{d}\|}$. It can be shown that $\hat{d}$ is uniformly distributed over the unit sphere. $\hat{d}$ was kept if its local elevation as measured from $\mathrm{r}_0 = \begin{bmatrix} R & 0 & 0 \end{bmatrix}^T$ was positive and re-drawn otherwise
3. The initial velocity was set to $\mathbf{r}_0' = v\hat{d}$

The plate is located at 0° longitude and 0° latitude at take-off, which corresponds to the following coordinates in the body-frame:

$$\mathbf{r}_0 = \begin{pmatrix} R \\ 0 \\ 0 \end{pmatrix} \tag{66}$$

The Sun was thus at the zenith of the plate's starting point. A simple eclipse model was added by formulating two necessary eclipse conditions.

$$\mathbf{r}^T\hat{s} < 0 \tag{67}$$

$$\|\left(I_3 - \hat{s}\hat{s}^T\right)\mathbf{r}\| < R \tag{68}$$

$$\tag{69}$$

The first condition translates into the plate flying over the far side of the asteroid with respect to the terminator. The second condition indicates that the plate lies within a cylinder of axis $\hat{s}$ and radius R. The plate is thus in the shadow of the asteroid if both conditions are met. These are summarized along with the rest of the observation geometry on Figure 30.

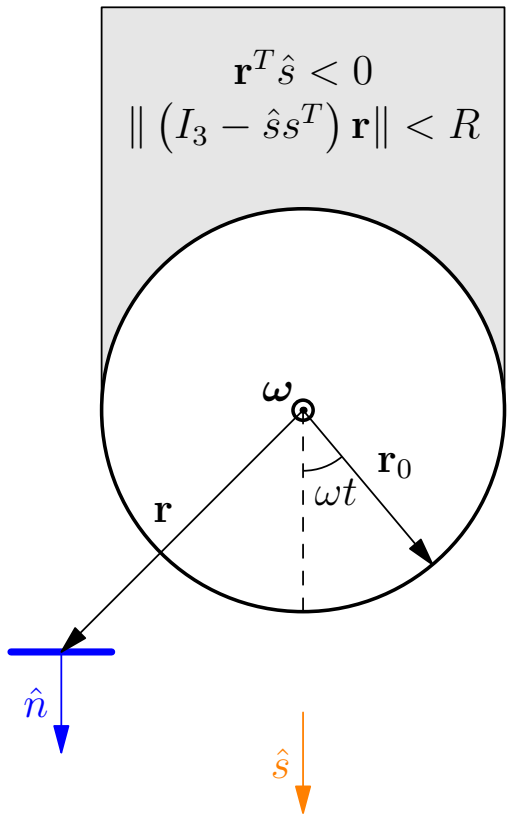

Figure 30: Lift-off geometry. The asteroid is modeled as a sphere of radius R. The plate retains a constant inertial attitude throughout its flight as it remains pointed at the sun. The shaded region on the backside of the asteroid depicts the eclipse area

4.3.2 Numerical example

A numerical simulation was run to assess the effect of SRP on near-surface post-hoping motion, implementing the eclipse model as well as the dynamics previously discussed.

The simulation inputs were set to the values shown in Table 6 and Table 7. 4000 samples of $\mathbf{r}_0'$ were drawn and applied to the plate, without and with SRP.

Property	Value	Unit
R	246	m
μ	5.2	m^3/s^{-2}
$\frac{2\pi}{\omega}$	4.297812	hours

Table 6: Bennu geophysical state as found in [39]

Property	Value	Unit
ρ	1	–
δ	0	–
σ	0.5	m^2/kg
Φ	1000	W/m^2

Table 7: Plate and SRP environment characteristics

Two initial magnitudes v were investigated: $v = 1$ cm/s and $v = 10$ cm/s. Corresponding results are shown on Figure 31 and Figure 32, along with a color chart indicating the euclidian distance between the take-off location and the impact points. Trajectories were labelled as impacting if their radius became strictly less than R at any time during the simulation, that spanned 10 hours.

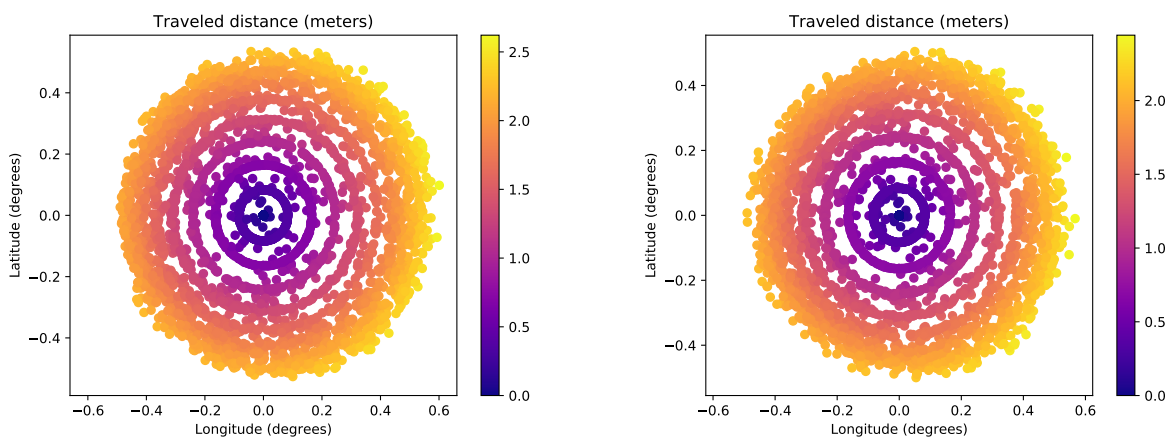

Figure 31: Impact map for $v = 1$ cm/s, without SRP (left) and with SRP (right)

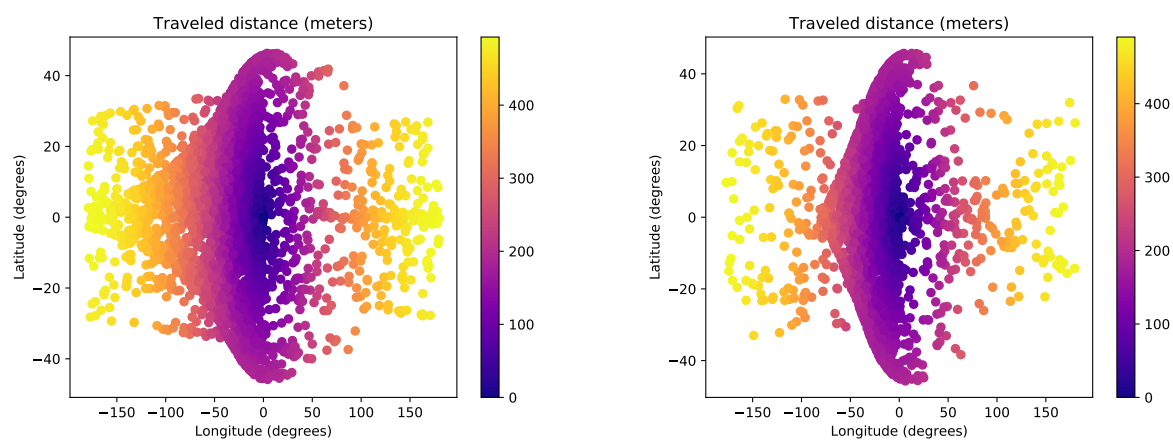

Figure 32: Impact map for $v = 10$ cm/s, without SRP (left) and with SRP (right)

Figure 31 denotes a nearly identical clustering of the impact trajectories when the imparted impulse has a magnitude of 1 cm/s, as SRP does not significantly change the impact pattern. The circular stripes

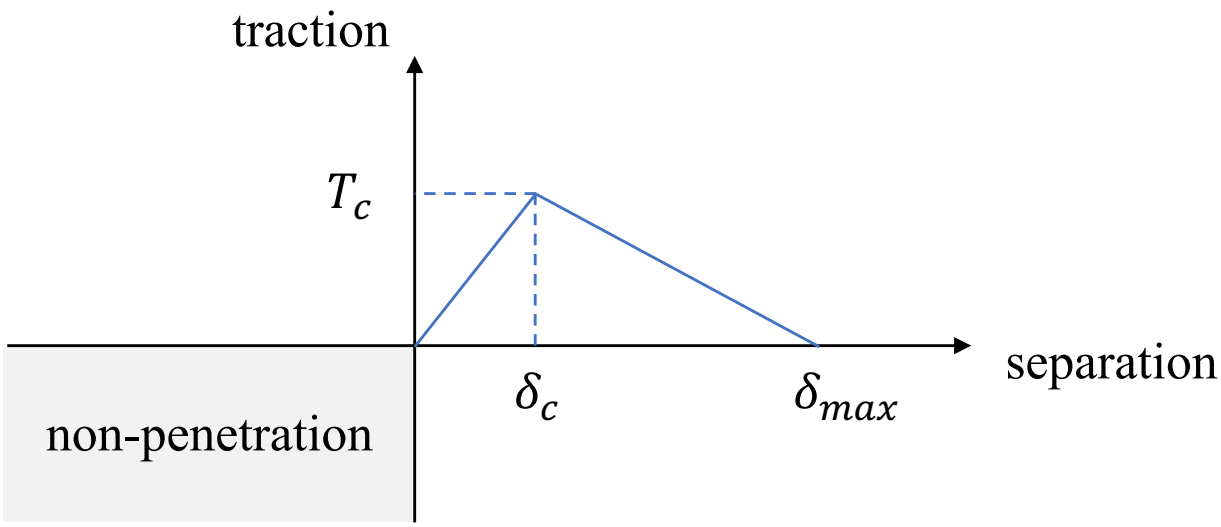

Figure 33: Contact Cohesion Law

that can be seen around the departure point $(0°, 0°)$ are nothing more but a numerical artifact: they are a conjunction of the finite precision in the impact radius detection, the asteroid curvature and the projection of the position to the longitude/latitude space. In either case, the maximum travelled distance did not exceed 2.5 meters.

On the other hand, increasing the impulse magnitude to $v = 10$ cm/s yields dissimilar results. First, the impact patterns are clearly not symmetric in longitude, which is a consequence of the asteroid rotation about its pole. In addition, Figure 32 shows impacting patterns that differ greatly when SRP is turned on. This makes complete sense as a larger impulse provides the plate with more 'air time' over which SRP can act. Scheeres et al.'s minimum estimate of Bennu's escape speed is $v_{esc} = 13$ cm/s at the equator [39]. The escape speed encompasses the spin rate, surface orientation, total gravity field of the system and assumes a departure direction normal to the surface. Because our simulation did not constrain the initial impuse $\mathbf{r}_0'$ to be normal, it is not guaranteed that all the departure trajectories will remain bounded. In fact, turning on SRP in this case caused a number of trajectories to escape.

The major take-away of this study is that SRP could bring in controlability to the post-hop motion, as revealed by the clustering in the impact points. There is potential benefit in harnessing SRP to navigate about the central body. To this end, specific control policies more elaborate than $\hat{n} \equiv \hat{s}$ would of course need to be devised.

4.4 Locomotion Feasibility Study

The goal of this study is to analyze different modes of locomotion of a robot on the asteroids surface. The robot is assumed to be of a smart, self-actuated material. Two fundamentally different locomotion modes are considered: (a) a crawling type motion that resembles the motion of caterpillar, and (b) a jumping motion. The interaction of the robot with the asteroids surface is simplified to mechanical contact and cohesion. Gravity and other environmental forces are neglected.

The adhesion law describing the traction between the robot and the surface is modeled by a simple bi-linear relation as shown in Figure 33. This simplified law approximates the simulation results reported in Sanchez and Scheeres [46]. For a positive separation distance, the peak traction Tc is reached at a separation c. The traction vanishes for a separation distance larger than max. The values for the maximum traction and separation c were taken from [46]. Note that these values are computed for cohesion between asteroid surface material.

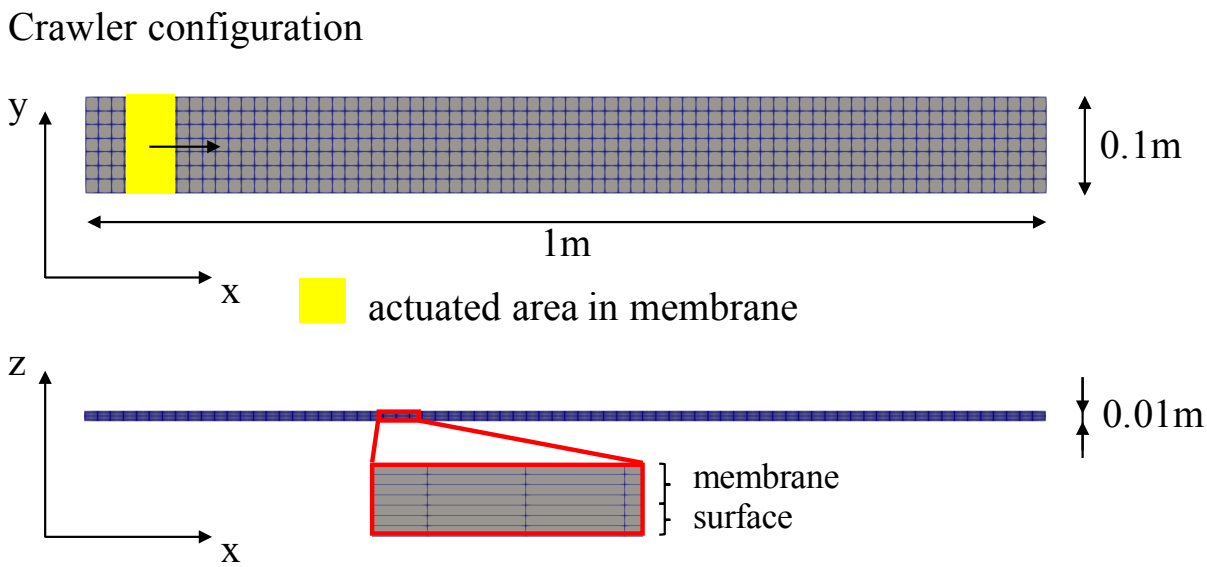

Figure 34: Crawler configuration

Property	Value
Young's modulus	$3 \cdot 10^6$ N/m2
Poisson ratio	0.45
Density	103 kg/m3
Mass proportional damping coefficient	100.0
Membrane substrate thickness	0.00625 m 0.00375 m
Maximum cohesion	250 N/m2
Separation at maximum cohesion	0.01 m
Separation at zero cohesion	0.10 m
Velocity of actuated strip	0.1 m/s

Table 8: Crawler configuration

The robot is modeled as a rectangular or square membrane for the crawler or the jumper configurations, respectively. Finite element models of these configurations along with dimensions are shown in Figures 34 and 35. The membranes and the asteroids surface are modeled by 3D hexagonal elements assuming a linear elastic behavior. The actuation is described by a thermal analogy. In parts of the membrane a time-varying temperature gradient is imposed across the membrane thickness, resulting in a bending moment and in-plane force. Damping is modeled using a mass-proportional approach based on the Rayleigh damping model. The nominal material parameters and cohesion law coefficient are given in Tables 8, 9 and 10.

For the crawler configuration the thermal gradient is ramped up to is maximum value over 20.0 ms which corresponds to a thermal-equivalent strain of 0.1; after that time the actuated strip was moved in horizontal direction (x-direction) with a speed of 0.1 m/s. For the jumper configuration, the thermal gradient is also ramped up over 20.0 ms to its maximum eigenstrain value of 0.1. The dynamic response of the configurations is analyzed by a generalized Newmark- method using a constant time step size of 1.0 ms.

Figures 36 and 37 show snapshots of the simulations for the material parameters given in Tables 8, 9 and 10. Figure 36 shows that the self-actuation represented by the thermal strain model is capable to overcome the cohesive forces and travel along the membrane. Note the assumption of a linear kinematic does not allow for a realistic simulation of the caterpillar motion. However, the simulations confirm that the concept

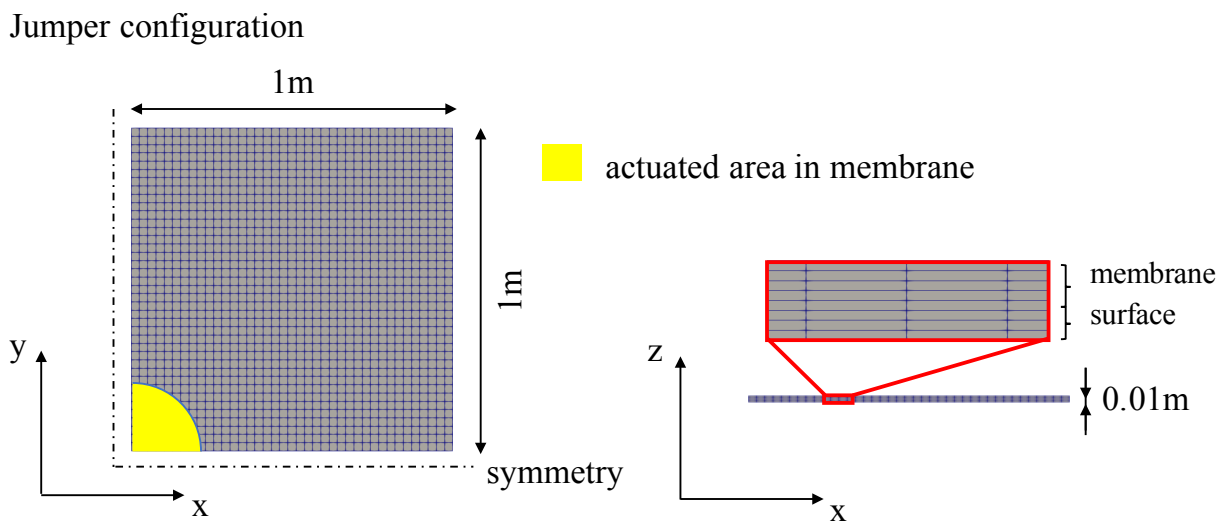

Figure 35: Jumper configuration

Property	Value
Young's modulus	$5 \cdot 10^7$ N/m2
Poisson ratio	0.45
Density	103 kg/m3
Mass proportional damping coefficient	100.0
Membrane substrate thickness	0.0055 m 0.0045 m
Maximum cohesion T_c	250 N/m2
Separation at maximum cohesion δ_c	0.01 m
Separation at zero cohesion $\delta_{\max}$	0.10 m
Radius of actuated patch	0.1 m

Table 9: Jump-Off configuration

if feasible given sufficient actuation moments.

Figure 37 shows the jumper configuration considering two actuation modes: the top surface of the membrane within the actuated region (a) expands and (b) contracts. In both cases the impulse load created by the interaction of the actuation and the subtract surface is sufficient to let the robot overcome the adhesion and to move beyond the maximum separation distance. While the transient response of the membrane depends on whether the actuated region expands or contracts, the overall motion is rather similar. To gain insight in the dependency of the transient response of the membrane on its mechanical properties and the actuation mode different values for the membrane Youngs modulus, damping values, magnitudes of eigen stains and sizes of the actuated patch were studied. The main findings are summarized below:

- For the crawler motion, it is important that the Youngs modulus of the membrane is rather small, i.e. at the level of an elastomer. If the Youngs modulus is too large, the adhesive forces are insufficient to pull back the membrane to the surface and the robot may lift of depending on the strength of the impulse created by the initial actuation.
- For the jumper motion, a higher Youngs modulus is beneficial, e.g. that of a silicon rubber.
- For both configurations, material damping plays an important role such that higher frequencies damp out quickly. These frequencies are generated by the initial application of the actuation forces.

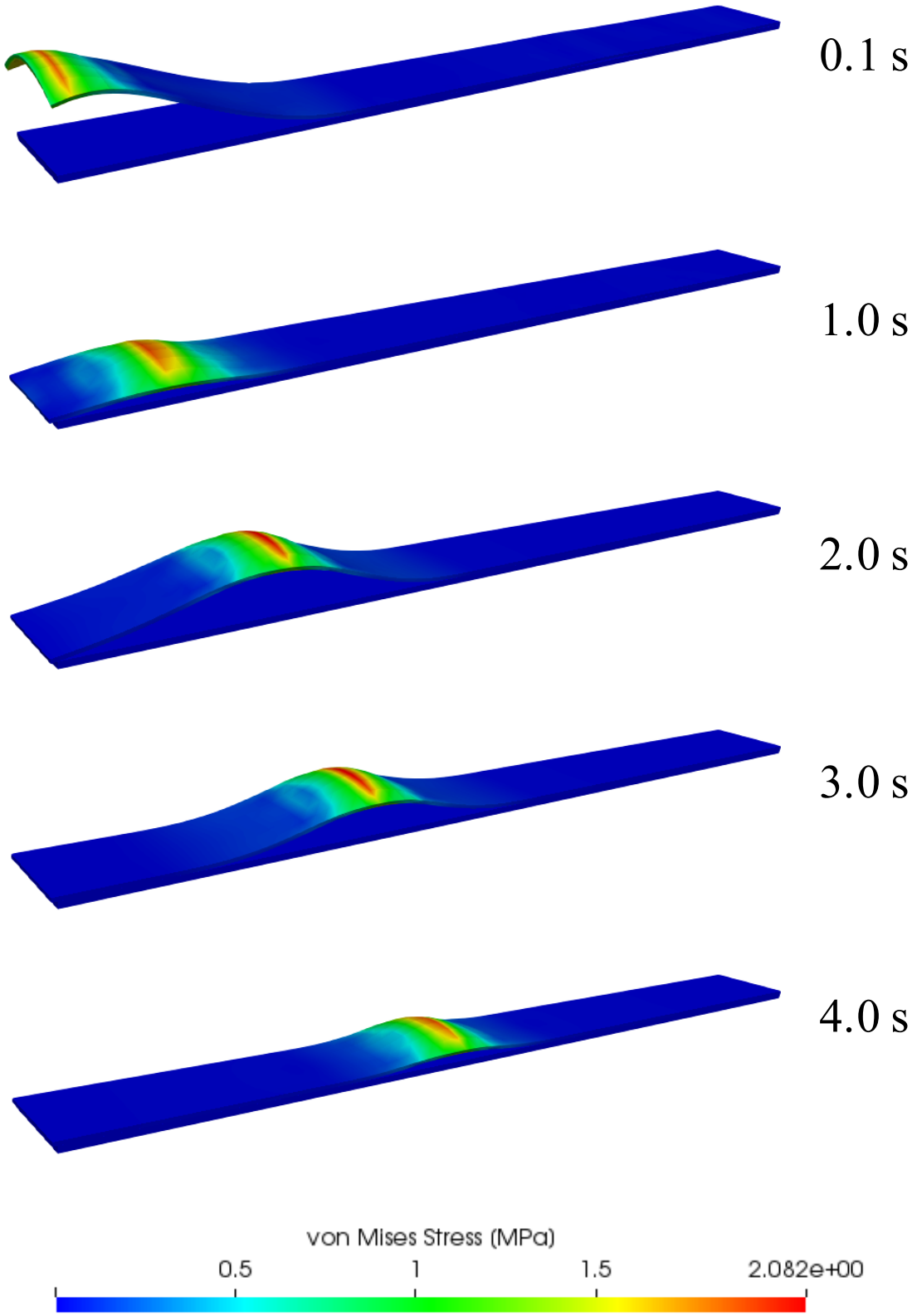

t

Figure 36: Snapshots of deformations of crawler configurations with von Mises stress contours

Property	Value
Young's modulus	$\cdot 10^5$ N/m2
Poisson ratio	0.25
Density	$2 \cdot 10^3$ kg/m3

Table 10: Surface properties

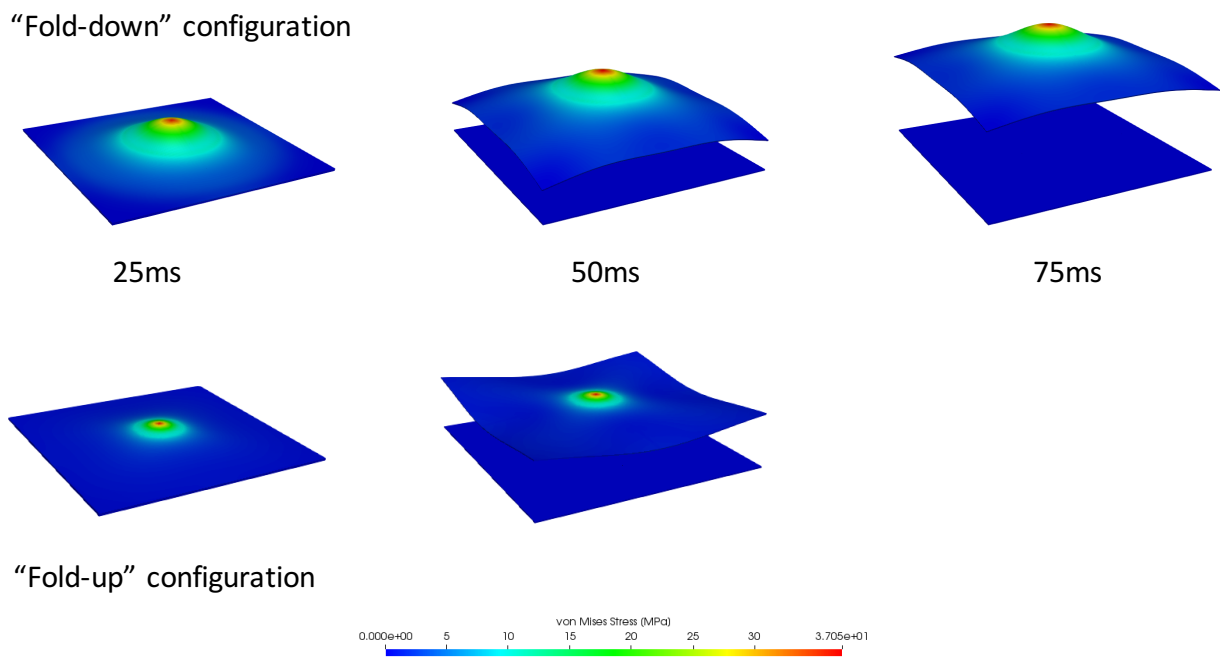

t

Figure 37: Snapshots of deformations of Jumper configuration; von Mises stress contours; top row: fold-down actuation; bottom row: fold-up actuation.

- The magnitude of the actuation forces and moments, as well as the size of the actuated region, need to be tailored to the mechanical properties of the membrane. This is important for the crawler configuration as small actuation may lead to insufficient separation and large actuation may result in the robot lifting of the surface.

5 Materials

5.1 Limb Material Selection

A soft robot moving about the surface of an asteroid must be well protected from harsh terrain. Some form of a flexible material will need to line the underside of the limbs to protect sensitive electronics and actuators that allow the spacecraft to move. The chosen material will need to be tolerant of space environment factors such as temperature, radiation, and pressure, but will also need to be flexible enough to allow the spacecraft limbs proper functionality. The group of polymers known as silicone elastomers offer a possible solution to the issue of material selection.

Silicone elastomers have a history of use in space due to their low rates of outgassing and resilience to temperature and radiation extremes. On Earth they are sometimes used in the manufacturing of cables for nuclear power plants [45]. de Groh III et al. studied three specific silicone elastomers for use as o-ring

sealants in spacecraft: Esterline ELA-SA-401, Parker Hannifin S0383-70, and Parker Hannifin S0899-50. The study included thermal, radiation, and pressure testing of each elastomer, finding each suitable for the space environment. Each of these elastomers is classified as a low-outgassing compound per NASA's ASTM E 595.

Additional polymers with a history of space application that may be useful for protecting the spacecraft limbs include flexible epoxies, polyurethanes, acrylics, and fluorocarbons [15]. More rigorous testing will be required to make a final determination of the optimal polymer for protecting the spacecraft limbs. One critical factor requiring further testing is the natural adhesion the polymer will have with asteroid regolith due to Van der Waals force.

5.2 Adhesion

It has been well established at this point that van der Waals cohesion plays a major role in holding rubble pile asteroids together[38], in some cases keeping an asteroid from ripping apart due to centripetal accelerations[34]. Their effect on rubble pile asteroids is especially significant due to the microgravity environment at the surface. These van der Waals forces are nature's solution to overcoming the difficulties of interacting with a small NEA surface. AoES are designed to use van der Waals forces to create a controllable method of adhesion between the spacecraft structure and the asteroid, similar to how geckos [3] walk up walls. This situation is depicted in the illustration shown in Fig. 38. In this environment, the centripetal accelerations on the surface, caused by the spin of the asteroid, $\boldsymbol{\omega}$, can equal or overcome the net gravitational force at the surface. The cohesive forces between the components of the rubble pile asteroid help to hold it together. AoES will take advantage of similar physics to keep from flying off the surface - due to centripetal accelerations or from reaction forces from moving or otherwise interacting with the surface.

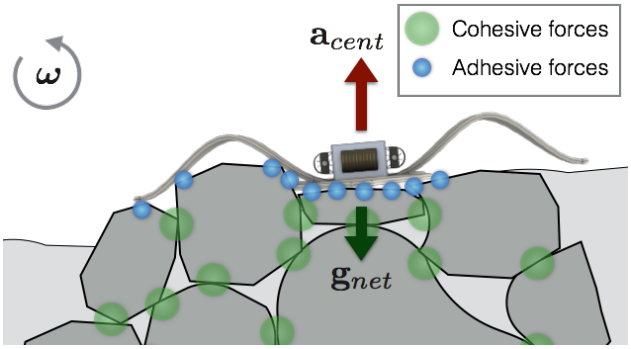

Figure 38: Diagram illustrating the forces acting in the microgravity environment on the surface of a small rubble-pile asteroid.

The initial conceptual design for AoES is a large area soft robotic surface, with a small, low profile bus structure centered on the top. The soft robotic structure is made of a flexible material, such as a silicone rubber, which allows for accommodation of rough asteroid surfaces [1, 7, 36] while keeping significant surface area in contact. Furthermore, the flexible structure can be actuated - a necessary component for enabling surface mobility. This is inspired by existing soft robots developed and demonstrated in terrestrial environment, such as those pictured in Fig. 39.

Figure 39: Three existing soft robots showing various forms of locomotion similar to what is proposed here (left[22], center[21], right[35]).

Van der Waals forces are only effective over very short distances, and the total adhesive strength depends

on the total number of contacts between the two surfaces as

$$\sigma_y = \frac{N_c f_c}{A_b} \tag{70}$$

where N_c is number of contacts, A_b is area of each contact, and f_c is the cohesive force, which is determined from

$$f_c = A_h r_1 r_2/(r_1 + r_2) \tag{71}$$

where A_h is the Hamaker constant which has a value of 0.036 N m^{-1} [31] for lunar surfaces. In [38], a scaling law was developed and empirically determined for the cohesive strength of randomly packed grains as

$$\sigma_y = \frac{1.56 \times 10^{-4}}{\bar{r}_p} \tag{72}$$

where the average grain size, $\bar{r}_p$, was simulated as 0.0125 m, which gives a strength of 0.0125 Pa. By this scaling law, as the average grain size get smaller, the strength goes up. Recent literature has found that rubble pile asteroids should have cohesion on the order of magnitude of 1-10^2 Pa [34, 38], which is similar to the value for lunar regolith of around 10^2 Pa [31]. Thus smaller grains must be present to provide this level of strength. Furthermore, according to Eq. (71), assuming similar sized grains is actually a conservative assumption that provides a lower bound to the strength. In fact, if one object is larger than the other, the strength will increase, causing smaller grains to become preferentially attracted to larger objects.

As a simple example of the force that cohesion can produce, if we assume that the cohesive force is 10 Pa, then over a 1-m area (with the same number of contacts as in regolith) this produces a net 10 N force. At the equator of a 250 m radius asteroid with Bennu's mass[9], spinning with a period of 3.085 hours such that the centripetal acceleration ($r\omega^2$) equals gravity (μ/r^2), a 100 kg spacecraft with it's center of mass 0.5 m above the surface would experience a centripetal force away from the surface of 1.6×10^{-5} N.

Thus, if flexible material can be found which produces adhesion at even a small fraction of the strength of regolith cohesion, AoES will have no problem anchoring to the surface of a rubble pile asteroid! Assuming a constant number of average contacts per area, increasing the area of the AoES will increase the adhesive force that can anchor the spacecraft to the surface. Any excess adhesive capability can be used to anchor the AoES so that it can interact with the surface (for digging etc) without launching itself off of the asteroid.

In order for AoES to be able to move across the surface, we again take inspiration from nature in how animals which rely on adhesion or large surface areas for locomotion (such as slugs or caterpillars) move, as those designs in Fig. 39 and others [48, 21] have previously. The fast application of localized internal forces allows the adhesion of that area to be broken. When done in particular sequences, this allows the AoES to crawl across the surface. This type of undulating motion seen in caterpillars has been studied for terrestrial applications[22] where the robot had a aspect ratio greater than one. For our applications, it may be more desirable to have a circular or square shape - thus other more complex motions which combine this undulation with motion similar to a spinning disc moving across a surface may be a useful extension here.

5.3 Electroadhesion

In addition to passive adhesion provided by Van der Waals forces, utilizing electroadhesion will allow the spacecraft to actively control its adhesion to the surface of asteroids. By planting alternating electrodes into the protective polymer of the spacecraft's limbs, a charge can be induced on whatever surface is in contact with the polymer, as demonstrated in Figure 40. This induced charge creates an attraction between the electrodes and surface, resulting in a clamping effect.

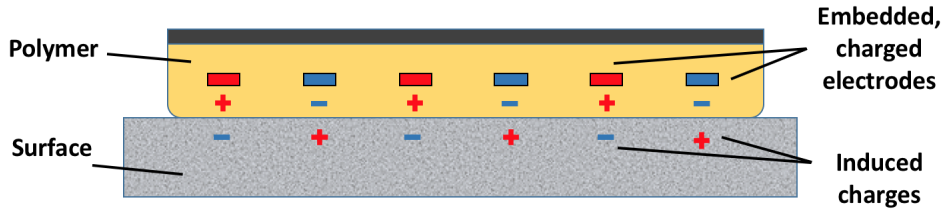

Figure 40: Example diagram of electrodes imbedded in a polymer generating an electroadhesive force between the polymer and a surface

The use of electroadhesion provides many benefits to the mission. Induced charge is a function of voltage, therefore electroadhesion allows for fully controllable levels of adhesion. Electroadhesion works on many different surfaces, whether dusty or clean, and is not limited to use in any specific type of polymer [33]. Additionally, as Prahlad et al. found, electroadhesion can be applied for only 0.02 milliWatts per Newton supported. This level of power is easily achievable by typical spacecraft power budgets.

The primary drawback of utilizing electroadhesion is the need to appropriately control the array of electrodes. Electroadhesion could help a spacecraft move, toss boulders, and perform many other mobility-related tasks on asteroid surfaces, but all of these actions would require careful control of electroadhesion. Understanding how this effect can be utilized to assist in these activities will be a goal of future development.

5.4 Adhesion experiments

One of the main goals of the NIAC proposal is to quantify the van der Waals adhesive force between the flexible AoES limb material and the asteroid regolith. A drop tower test and a tensile pull test were designed to accomplish this feat. Figure 41 shows the preliminary design for a drop tower experiment. By controlling the tower acceleration, a micro-gravity or negative-gravity environment is created in the test chamber. In order for this experiment to be successful, there needs to be a gravity differential between the AoES material and the regolith. This means that the regolith will be secured to the base of the test chamber. During the experiment, a high-speed camera is used to determine when the AoES material separates from the asteroid regolith. This experiment will be able to determine the force necessary to separate the AoES material from the asteroid regolith, which is a function of material type, regolith properties, test sample area, and test sample mass, by cataloging the gravity differential necessary for material separation.

Figure 42 shows the preliminary design for a tensile pull experiment. A coating of the chosen AoES material is applied to a stiff aluminum substrate, which is then attached to a high precision force gauge. A pulley system will then impart an evenly distributed force onto the AoES material pulling it up from the regolith while the force gauge measures the process. This experiment will be able to directly measure the adhesive force between the AoES material and the regolith, which will again depend on material type, regolith properties, test sample area, and test sample mass. In order to get an accurate measurement, a "dry run" would first be performed with no regolith in order to calibrate the force gauge. Using these two experiments, the adhesive force between the AoES limb material and asteroid regolith will be accurately characterized.

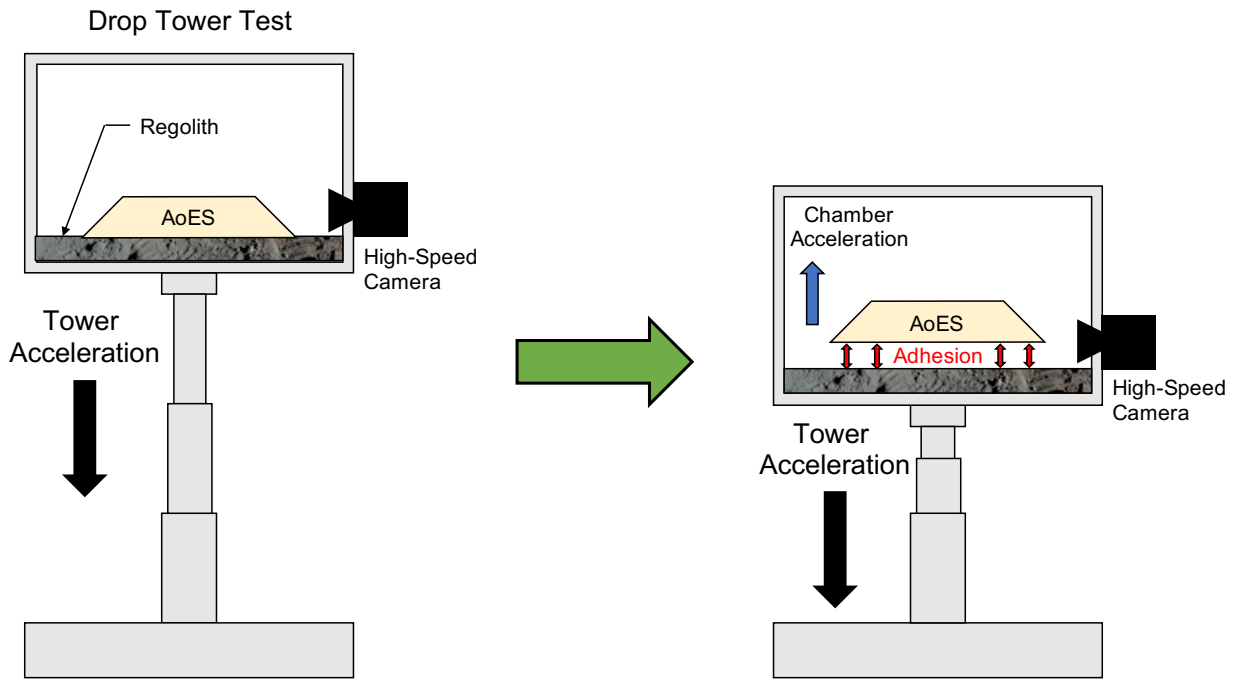

Figure 41: This figure shows a preliminary configuration for a drop tower experiment to measure the adhesive force between the AoES material and asteroid regolith.

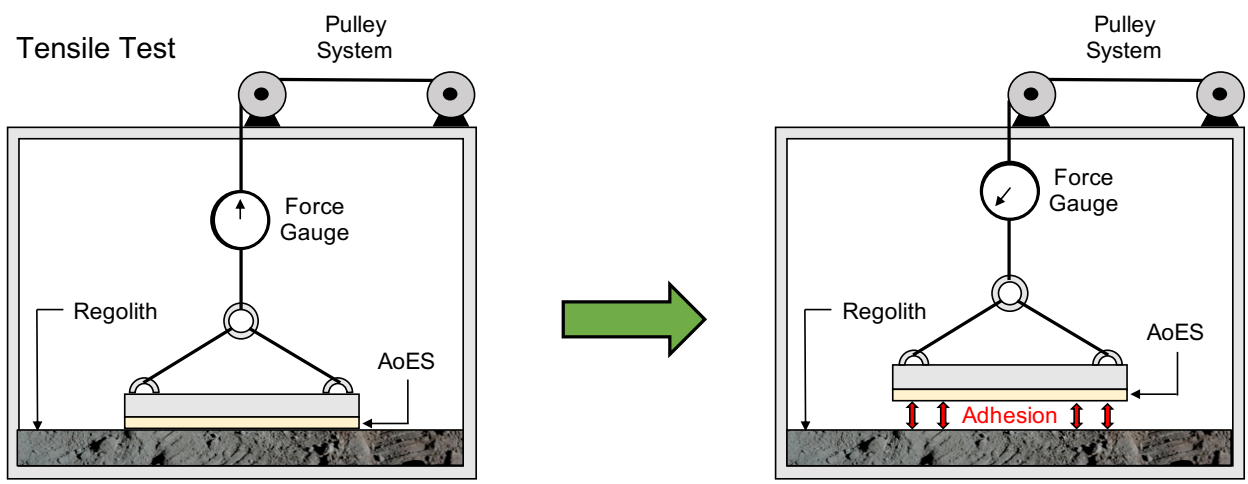

Figure 42: This figure shows a preliminary configuration for a tensile pull experiment to measure the adhesive force between the AoES material and asteroid regolith.

6 Conclusions from Phase I

The Phase I study was focused on the major uncertainties in the basic feasibility of this concept, which fell into four categories: mission and system design, mobility, actuation, and materials. The motivating questions for Phase I, and brief summary of the results are:

Mission and System Design: What are realistic size, power, mass, and shapes for the AoES? Basic system designs have been developed that produce an area-to-mass ratio in the range of 0.1-0.5 m^2/kg.

Mobility: Are the crawling, hopping, and landing processes possible as imagined in the Phase I proposal? In short, yes. Computational mechanics model show that both crawling and hopping are possible. Simulations of orbit and hopping control leveraging SRP forces indicate significant controllability is available with the area-to-mass ratios achieved in the system design.
Actuation: Is it possible to actuate the soft robotic material as is necessary for the mobility concepts we want? Do actuators with enough strength and control with realistic power exist? Will they function while dirty? This project has been greatly improved by combining forces with Co-I Keplinger to use his HASEL actuators. These actuators allow us to answer yes to all of the previous questions and provide significant flexibility and performance in the AoES design.
Materials: Are there any possible materials that can be used? Will adhesion exist for these materials? Can the material be kept from turning to glass? Silicone elastomer has some heritage for space applications and is our leading material. While the question of adhesion remains open, our design now incorporates electroadhesion which means the need for naturally arising van der Waals adhesive forces is not as necessary for feasibility. Possible thermal control solutions have been identified but require more testing.

In short, our work has indicated that not only are there no major issues at this stage, but that there is even more promise to this concept than originally thought! However, there are still a number of outstanding questions that must be answered to ensure concept feasibility:

- **Is** adhesive anchoring actually useable?
- **Can** HASEL actuators be used in space?
- **Will** the digging and launching process work as predicted?
- **Can** the soft robotic materials be kept at proper operating temperatures?
- **Can** the AoES actually be autonomously steered to arrive safely on the asteroid surface?
- **Can** the soft robotic leg designs actually be built and actuated?

Given the promise and massive upside of this concept, we believe further research and development should be directed toward the AoES concept.

References

[1] Shinsuke Abe, J Saito, H Miyamoto, Tadashi Mukai, R Nakamura, Naru Hirata, Olivier S Barnouin-Jha, M Ishiguro, T Michikami, Andrew F Cheng, A M Nakamura, Hirohide Demura, H Demura, Robert W Gaskell, S Sasaki, Tatsuaki Hashimoto, Kensuke Hiraoka, N Hirata, Takayuki Honda, C Honda, Takashi Kubota, A Yamamoto, Y Yokota, Masatoshi Matsuoka, T Fuse, Takahide Mizuno, Ryosuke Nakamura, F Yoshida, Daniel J Scheeres, D J Tholen, R W Gaskell, Makoto Yoshikawa, T Hashimoto, T Kubota, Y Higuchi, T Nakamura, P Smith, K Hiraoka, T Honda, S Kobayashi, M Furuya, N Matsumoto, E Nemoto, A Yukishita, K Kitazato, B Dermawan, A Sogame, J Terazono, C Shinohara, and H Akiyama. Mass and Local Topography Measurements of Itokawa by Hayabusa. Science, 312(5):1344–1349, June 2006.

[2] E Acome, SK Mitchell, TG Morrissey, MB Emmett, C Benjamin, M King, M Radakovitz, and C Keplinger. Hydraulically amplified self-healing electrostatic actuators with muscle-like performance. Science, 359(6371):61–65, 2018.

[3] Kellar Autumn and Anne M Peattie. Mechanisms of Adhesion in Geckos. Integrative and Comparative Biology, 42(6):1081–1090, December 2002.

[4] Jens Biele, Stephan Ulamec, Michael Maibaum, Reinhard Roll, Lars Witte, Eric Jurado, Pablo Muñoz, Walter Arnold, Hans-Ulrich Auster, Carlos Casas, Claudia Faber, Cinzia Fantinati, Felix Finke, Hans-Herbert Fischer, Koen Geurts, Carsten Güttler, Philip Heinisch, Alain Herique, Stubbe Hviid, Günter Kargl, Martin Knapmeyer, Jörg Knollenberg, Wlodek Kofman, Norbert Kömle, Ekkehard Kührt, Valentina Lommatsch, Stefano Mottola, Ramon Pardo de Santayana, Emile Remetean, Frank Scholten, Klaus J. Seidensticker, Holger Sierks, and Tilman Spohn. The landing(s) of Philae and inferences about comet surface mechanical properties. Science, 349(6247):1–7, 2015.

[5] William F Jr Bottke, David Vokrouhlický, David P Rubincam, and David Nesvorný. The Yarkovsky and Yorp Effects: Implications for Asteroid Dynamics. Annual Review of Earth and Planetary Sciences, 34(1):157–191, May 2006.

[6] Daniel N Brack and Jay W McMahon. Dynamical behavior of an asteroid undergoing material removal. In 2018 Space Flight Mechanics Meeting, page 0954, 2018.

[7] Andrew F Cheng, O Barnouin-Jha, L Prockter, M T Zuber, G Neumann, D E Smith, J Garvin, M Robinson, J Veverka, and P Thomas. Small-Scale Topography of 433 Eros from Laser Altimetry and Imaging. Icarus, 155(1):51–74, January 2002.

[8] Steven R Chesley, Paul W Chodas, Andrea Milani, Giovanni B Valsecchi, and Donald K Yeomans. Quantifying the Risk Posed by Potential Earth Impacts. Icarus, 159(2):423–432, October 2002.

[9] Steven R Chesley, Davide Farnocchia, Michael C Nolan, David Vokrouhlický, Paul W Chodas, Andrea Milani, Federica Spoto, Benjamin Rozitis, Lance A M Benner, William F Bottke, Michael W Busch, Joshua P Emery, Ellen S Howell, Dante S Lauretta, Jean-Luc Margot, and Patrick A Taylor. Orbit and bulk density of the OSIRIS-REx target Asteroid (101955) Bennu. Icarus, 235(C):5–22, June 2014.

[10] N Correll and R Voyles. Robotic Materials: From smart polymers to computational metamaterials. Proc Robot Makers Workshop, 2014.

[11] Nikolaus Correll, Çağdaş D Önal, Haiyi Liang, Erik Schoenfeld, and Daniela Rus. Soft Autonomous Materials—Using Active Elasticity and Embedded Distributed Computation. In Experimental Robotics, pages 227–240. Springer Berlin Heidelberg, Berlin, Heidelberg, 2014.

[12] Harry Dankowicz. Some special orbits in the two-body problem with radiation pressure. Celestial Mechanics & Dynamical Astronomy, 58(4):353–370, 1994.

[13] S Diaham, S Zelmat, M-L Locatelli, S Dinculescu, M Decup, and T Lebey. Dielectric breakdown of polyimide films: Area, thickness and temperature dependence. IEEE Transactions on Dielectrics and Electrical Insulation, 17(1), 2010.

[14] M L Gobinddass, P Willis, O De Viron, A Sibthorpe, N P Zelensky, and J C Ries. Improving DORIS geocenter time series using an empirical rescaling of solar radiation pressure models. Advances in Space Research, 44:1279–1287, 2009.

[15] E. Grossman and I. Gouzman. Space environment effects on polymers in low earth orbit. Nuclear Instruments and Methods in Physics Research, 208, 2003.

[16] Loura Hall. Soft-Robotic Rover with Electrodynamic Power Scavenging. May 2015.

[17] W W James, K Zacny, J Craft, P Chu, and M M Cohen. Robotic Asteroid Prospector (RAP) NIAC Phase 1 Results. In AIAA SciTech. 7th Symposium on Space Resource . . . , 2014.

[18] Jun'ichiro Kawaguchi, Akira Fujiwara, and Tono Uesugi. Hayabusa-Its technology and science accomplishment summary and Hayabusa-2. Acta Astronautica, 62(10-11):639–647, 2008.

[19] Nicholas Kellaris, Vidyacharan Gopaluni Venkata, Garrett M Smith, Shane K Mitchell, and Christoph Keplinger. Peano-hasel actuators: Muscle-mimetic, electrohydraulic transducers that linearly contract on activation. Science Robotics, 3(14):eaar3276, 2018.

[20] Christoph Keplinger, Martin Kaltenbrunner, Nikita Arnold, and Siegfried Bauer. Capacitive extensometry for transient strain analysis of dielectric elastomer actuators. Applied Physics Letters, 92(19):192903, 2008.

[21] Huai-Ti Lin, Gary G Leisk, and Barry Trimmer. GoQBot: a caterpillar-inspired soft-bodied rolling robot. Bioinspiration and Biomimetics, 6(2):026007–, June 2011.

[22] C Majidi, R F Shepherd, R K Kramer, G M Whitesides, and R J Wood. Influence of surface traction on soft robot undulation. The International Journal of Robotics Research, 32(13):1577–1584, November 2013.

[23] Daniel D Mazanek, Raymond G Merrill, Scott P Belbin, David M Reeves, Bo J Naasz, Paul A Abell, and Kevin Earle. Asteroid Redirect Robotic Mission: Robotic Boulder Capture Option Overview. In AIAA SPACE 2014 Conference and Exposition, pages 1–22, Reston, Virginia, August 2014. American Institute of Aeronautics and Astronautics.

[24] M A McEvoy and N Correll. Materials that couple sensing, actuation, computation, and communication. Science, 347(6228):1261689–1261689, March 2015.

[25] M A McEvoy and N Correll. Thermoplastic variable stiffness composites with embedded, networked sensing, actuation, and control. Journal of Composite Materials, 49(15):1799–1808, June 2015.

[26] Colin R McInnes. Solar Sailing. Praxis Publishing, 1999.

[27] Jay W McMahon and B Cheetham. Lofted Regolith Sampling of Small Bodies. In Space Resources Roundtable, Golden, CO, 2016.

[28] Philip T Metzger. Space development and space science together, an historic opportunity. Space Policy, 37(Part 2):77–91, August 2016.

[29] M Pavone. Spacecraft/Rover Hybrids for the Exploration of Small Solar System Bodies. Technical report, October 2012.

[30] Ron Pelrine, Roy Kornbluh, Qibing Pei, and Jose Joseph. High-speed electrically actuated elastomers with strain greater than 100%. Science, 287(5454):836–839, 2000.

[31] H A Perko, J D Nelson, and W Z Sadeh. Surface cleanliness effect on lunar soil shear strength. Journal of geotechnical and geoenvironmental engineering, 127(4):371–383, 2001.

[32] Panagiotis Polygerinos, Nikolaus Correll, Stephen A Morin, Bobak Mosadegh, Cagdas D Onal, Kirstin Petersen, Matteo Cianchetti, Michael T Tolley, and Robert F Shepherd. Soft robotics: Review of fluid-driven intrinsically soft devices; manufacturing, sensing, control, and applications in human-robot interaction. Advanced Engineering Materials, 2017.

[33] H. Prahlad, R. Pelrine, S. Stanford, J. Marlow, and R. Kornbluh. Electroadhesive Robots - Wall Climbing Robots Enabled by a Novel, Robust, and Electrically Controllable Adhesion Technology. 2008 IEEE International Conference on Robotics and Automation.

[34] Ben Rozitis, Eric MacLennan, and Joshua P Emery. Cohesive forces prevent the rotational breakup of rubble-pile asteroid (29075) 1950 DA. Nature, 512(7513):174–176, August 2014.

[35] Daniela Rus and Michael T Tolley. Design, fabrication and control of soft robots. Nature, 521(7553):467–475, May 2015.

[36] C T Russell, C A Raymond, A Coradini, H Y McSween, M T Zuber, A Nathues, M C De Sanctis, R Jaumann, A S Konopliv, F Preusker, S W Asmar, R S Park, R Gaskell, H U Keller, S MOTTOLA, T Roatsch, J E C Scully, D E Smith, P Tricarico, M J Toplis, U R Christensen, W C Feldman, D J Lawrence, T J McCoy, T H Prettyman, R C Reedy, M E Sykes, and T N Titus. Dawn at Vesta: testing the protoplanetary paradigm. Science, 336(6082):684–686, May 2012.

[37] Ryan Russell. Survey of Spacecraft Trajectory Design in Strongly Perturbed Environments. Journal of Guidance, Control, and Dynamics, 35(3):705–720, 2012.

[38] P Sánchez and Daniel J Scheeres. The strength of regolith and rubble pile asteroids. Meteoritics & Planetary Science, 49(5):788–811, May 2014.

[39] D J Scheeres, S G Hesar, S Tardivel, M Hirabayashi, D Farnocchia, J W Mcmahon, S R Chesley, O Barnouin, R P Binzel, W F Bottke, M G Daly, J P Emery, C W Hergenrother, D S Lauretta, J R Marshall, P Michel, M C Nolan, and K J Walsh. The geophysical environment of Bennu. Icarus, 276:116–140, 2016.

[40] Daniel J. Scheeres. Orbit Mechanics About Asteroids and Comets. Journal of Guidance, Control, and Dynamics, 35(3):987–997, 2012.

[41] Daniel J. Scheeres. Orbital Motion in Strongly Perturbed Environments: Applications to Asteroid, Comet and Planetary Satellite Orbiters. Number 66391. Springer, Chichester, UK, 2012.

[42] Joel Sercel. APIS: Asteroid Provided In-situ Supplies. In Small Bodies Assessment Group, pages 1–17, June 2016.

[43] Joel Sercel. Asteroid Provided In-situ Supplies (APIS):. Technical report, April 2016.

[44] Robert F Shepherd, Adam A Stokes, Rui M D Nunes, and George M Whitesides. Soft Machines That are Resistant to Puncture and That Self Seal. Advanced Materials, 25(46):6709–6713, October 2013.

[45] Shin-Etsu Silicone. Characteristic Properties of Silicone Rubber Compounds. https://www.shinetsusilicone-global.com/catalog/pdf/rubber_e.pdf, 2016. [Online; accessed 09-February-2018].

[46] P. Snchez and D. J. Scheeres. The strength of regolith and rubble pile asteroids. Meteoritics & Planetary Science, 49(5):788–811, 2014.

[47] Yu Takahashi and Daniel J. Scheeres. Small-Body Postrendezvous Characterization via Slow Hyperbolic Flybys. Journal of Guidance, Control, and Dynamics, 34(6):1815–1827, 2011.

[48] M T Tolley, R F Shepherd, and B Mosadegh. A resilient, untethered soft robot. Soft Robotics, 2014.

[49] D. A. Vallado. Fundamentals of astrodynamics and applications. Springer Science & Business Media, 2001.

[50] Robert A Werner and Daniel J Scheeres. Exterior gravitation of a polyhedron derived and compared with harmonic and mascon gravitation representations of asteroid 4769 castalia. Celestial Mechanics and Dynamical Astronomy, 65(3):313–344, 1996.

[51] Guang-Zhong Yang, Jim Bellingham, Pierre E. Dupont, Peer Fischer, Luciano Floridi, Robert Full, Neil Jacobstein, Vijay Kumar, Marcia McNutt, Robert Merrifield, Bradley J. Nelson, Brian Scassellati, Mariarosaria Taddeo, Russell Taylor, Manuela Veloso, Zhong Lin Wang, and Robert Wood. The grand challenges of science robotics. Science Robotics, 3(14), 2018.

[52] K Zacny, P Chu, J Craft, and M M Cohen. Asteroid mining. In AIAA SPACE 2013 Conference and Exposition, 2013.

[53] Kris Zacny, Philip Chu, Gale Paulsen, Magnus Hedlund, and Bolek Mellerowicz. Asteroids: Anchoring and Sample Acquisition Approaches in Support of Science, Exploration, and In situ Resource Utilization. Asteroids: Prospective Energy and Material Resources, (Chapter 12):287–343, 2013.